

# Nonlinear evolution of the Richtmyer–Meshkov instability

MARCUS HERRMANN<sup>1</sup>, PARVIZ MOIN<sup>2</sup>  
AND SNEZHANA I. ABARZHI<sup>3†</sup>

<sup>1</sup>Department of Mechanical and Aerospace Engineering, Arizona State University, Tempe, AZ, USA

<sup>2</sup>Center for Turbulence Research, Stanford, CA, USA

<sup>3</sup>The University of Chicago and Illinois Institute of Technology, Chicago, IL, USA

(Received 20 July 2005 and in revised form 12 June 2008)

We report analytical and numerical results describing the dynamics of the two-dimensional coherent structure of bubbles and spikes in the Richtmyer–Meshkov instability for fluids with a finite density ratio. The theory accounts for the non-local properties of the interface evolution, and the simulations treat the interface as a discontinuity. Good agreement between the analytical and numerical results is achieved. To quantify accurately the interface dynamics in the simulations, new diagnostics and scalings are suggested. The velocity at which the interface would move if it were ideally planar is used to set the flow time scale as well as the reference point for the bubble (spike) position. The data sampling has high temporal resolution and captures the velocity oscillations caused by sound waves. The bubble velocity and curvature are both monitored, and the bubble curvature is shown to be the relevant diagnostic parameter. According to the results obtained, in the nonlinear regime of the Richtmyer–Meshkov instability the bubbles flatten and decelerate, and the flattening of the bubble front indicates the multiscale character of the coherent dynamics.

---

## 1. Introduction

When a shock wave passes an interface between two fluids with different acoustic impedances, the misalignment of the pressure and density gradients results in a growth of the interface perturbations. This phenomenon is called the Richtmyer–Meshkov instability (RMI) (Richtmyer 1960; Meshkov 1969). RMI is often considered as the Rayleigh–Taylor instability (RTI) with an ‘impulsive’ acceleration (Kull 1991). The Richtmyer–Meshkov (RM) instability produces turbulent mixing of the fluids, which plays an important role in many physical and technological processes. Several representative examples are inertial confinement fusion, core-collapse supernova, impact dynamics of liquids, and supersonic combustion (Kull 1991; Glendinning *et al.* 2003; Robey *et al.* 2003; Miles *et al.* 2004). Reliable description of the turbulent mixing is a long-standing problem in fluid dynamics. One of the fundamental issues to be understood is the evolution of the large-scale coherent structure characterizing the RM mixing zone (Abarzhi 2001, 2002; Abarzhi, Nishihara & Glimm 2003). Our work reports the multiscale character of the coherent dynamics and suggests the diagnostics and scaling for its reliable quantification.

† Author to whom correspondence should be addressed: snezha@stanford.edu

According to observations, RMI develops when a shock wave refracts through a perturbed interface, whether it propagates from the light fluid to the heavy fluid or in the opposite direction (Meshkov 1969; Holmes *et al.* 1999). In the linear regime of the instability, the light fluid ‘impulsively’ accelerates the heavy fluid, and the amplitude of the perturbation grows at a constant rate (Richtmyer 1960; Meshkov 1969). If the shock propagates from the heavy to the light fluid, the phase of the perturbation also reverses (Holmes *et al.* 1999). The value of the initial growth rate is determined by the shock-interface interaction and by the baroclinic production of vorticity (Velikovich 1996; Wouchuk 2001*a*). In the nonlinear regime, the growth rate decreases, and the coherent structure of bubbles and spikes appears (Aleshin, Ganalii & Zaitsev 1988; Aleshin, Lazareva & Zaitsev 1990). The light (heavy) fluid penetrates the heavy (light) fluid in bubbles (spikes) and the spatial period of the structure is set either by the initial conditions or by the mode of fastest growth (Collins & Jacobs 2002; Chebotareva *et al.* 1999). Shear-driven instabilities create small-scale structures on the side of the evolving spikes (Matsuoka, Nishihara & Fukuda 2003; Zabusky *et al.* 2003; Jacobs & Krivets 2005). If the flow is two-dimensional and the amplitude of the initial perturbation is large, then the spatial period of the large-scale coherent structure may increase (Alon *et al.* 1995; Oron *et al.* 2001). Eventually, a mixing zone develops. In the turbulent mixing regime, the bubbles and spikes decelerate, and their positions are described by power law time-dependence with the exponents dependent on the density ratio (Schneider, Dimonte & Remington 1998; Dimonte 2000; Glendinning *et al.* 2003; Robey *et al.* 2003; Miles *et al.* 2004).

The evolution of the Richtmyer–Meshkov instability is far from completely understood. The dynamics of RMI is governed by the nonlinear Euler or compressible Navier–Stokes equations with the initial and boundary conditions at the fluid interface. The compressibility, the baroclinic production of vorticity, the nonlinearities, and the secondary instabilities make the interface dynamics essentially non-local and result in the development of singularities in the governing equations. The non-locality and singularities cause significant difficulties for theoretical and numerical studies of the Richtmyer–Meshkov instability (for more details see Velikovich 1996; Wouchuk 2001*a*; Wouchuk 2001*b*; Abarzhi 2001; Abarzhi 2002; Matsuoka *et al.* 2003; Abarzhi *et al.* 2003 and references therein).

Having started from the classical work of Richtmyer (1960), several impulsive models were suggested to describe the linear regime of RMI (Meyer & Blewett 1972; Vandenboomgaerde, Muegler & Gauthier 1998). These models could not accurately account for the influence of vorticity deposited by the initial shock (Velikovich 1996; Zabusky *et al.* 2003) and did not explain the observations completely. An adequate analytical description of the linear regime of RMI was found recently by Wouchuk (2001*a, b*). This theory considered the interactions between the interface and the transmitted and reflected wave fronts, accounted for the baroclinic vorticity production, and derived with high accuracy the growth rate of RMI in the cases of strong and weak shocks as well as for fluids with similar and highly contrasting densities. The necessity of considering the higher-order interactions for obtaining an adequate description of the linear regime of RMI (discussed, for instance, in Velikovich 1996 and Wouchuk 2001*a, b*) is one of the indications of the non-local character of the instability evolution.

The nonlinear dynamics of RMI is a long-standing problem (Kull 1991; Zabusky *et al.* 2003). This transitional stage of the instability is important to study because it bridges a gap between the linear regime, with the perturbation growth rate determined by the initial conditions, and the turbulent mixing regime, whose evolution is perhaps

independent of the initial conditions (Glendinning *et al.* 2003; Robey *et al.* 2003; Miles *et al.* 2004). In addition, most of existing experiments and simulations in RMI do not pass completely into the turbulent regime (Robey *et al.* 2003; Jacobs & Krivets 2005). To identify benchmarks for observations and to set reliable grounds for modelling of the RM mixing process, a trustworthy description of the nonlinear dynamics is required. A test case, for which the nonlinear dynamics can be described analytically and validated with experiments and simulations, corresponds to RMI developing from a small-amplitude initial perturbation, a so-called single-mode perturbation (Aleshin *et al.* 1988, 1990; Jacobs & Sheeley 1996; Collins & Jacobs 2002; Jacobs & Krivets 2005).

The evolution of RMI is characterized by two, in general, independent, length scales: the position of the bubble (spike) and the spatial period of the coherent structure, i.e. the amplitude and the wavelength of the front. For a long time the nonlinear dynamics of RMI (RTI) was considered as a single-scale problem, characterized entirely by the spatial period of the structure of bubbles and spikes (Sharp 1984). This idea was employed by Alon *et al.* (1995) and Oron *et al.* (2001) in a heuristic model balancing with adjustable parameters the flow inertia and drag. The free parameters of the model have been calibrated via a comparison with some of the observations; however, the models could not explain the results of all observations and were subjects of controversy (Schneider *et al.* 1998; Dimonte 2000; Robey *et al.* 2003; Miles *et al.* 2004). The assumptions of Alon *et al.* (1995) and Oron *et al.* (2001) agreed with a so-called single-mode solution obtained by Goncharov (2002). The single-mode solution presumed a local character of the interface evolution, and reported that the curvature of the bubble front is a finite constant value, independent of the density ratio and proportional to the inverse spatial period (Goncharov 2002). The non-local properties of the nonlinear dynamics of RMI were accounted for by the analysis based on group theory (Abarzhi 2001; Abarzhi *et al.* 2003), which has found that the curvature of the bubble front in RMI should approach zero asymptotically. This result indicates that two length scales, the wavelength and the amplitude of the front, contribute independently to the nonlinear dynamics, and the evolution of RMI has a multiscale character.

Is the nonlinear coherent dynamics in RMI a local process characterized entirely by a single length scale, as presumed by the single-scale models (Sharp 1984; Alon *et al.* 1995; Oron *et al.* 2001; Goncharov 2002)? Or is it a non-local and multiscale phenomenon, as follows from the group theory approach (Abarzhi 2001; Abarzhi *et al.* 2003)? Addressing this issue is crucial for understanding the nonlinear RMI and for a development of a sound phenomenological model of the turbulent mixing process.

Here we perform an accurate and systematic study of the nonlinear RMI with improved diagnostics. We obtain analytical and numerical results describing the nonlinear evolution of the two-dimensional coherent structure in RMI for fluids with a finite density ratio. Our theory applies the theoretical method of Abarzhi (2001) and Abarzhi *et al.* (2003) for the two-dimensional case and extends it to higher orders of approximation. Our simulations solve the Navier–Stokes equations using a fully compressible second-order hybrid tracking/capturing scheme. The numerical method treats the interface as a discontinuity, and is applicable for fluids with highly contrasting as well as similar densities. New diagnostics and scaling are used to quantify the interface dynamics accurately, and both the velocity and curvature of the bubble front are monitored. Our simulations have high temporal resolution and run for a time significantly longer than in other observations. Good agreement between

the theory and the simulations is achieved. According to our results, the shape of the bubble front is not determined uniquely by the spatial period of the coherent structure, and the nonlinear RM bubbles flatten and decelerate. The flattening and deceleration of the bubble front are inter-related processes, and they indicate the essentially non-local and multiscale character of RMI evolution. We show that, due to the compressible nature of RMI and a relatively short dynamic range of the observation time, it may be extremely challenging for experiments and simulations to verify the power law time-dependence of the velocity of the nonlinear RM bubble.

## 2. Theory

In the nonlinear regime of RMI, the interface evolves without external forces, the bubble and spike growth rates decrease with time, and the fluid motion is nearly incompressible. Let  $t$  be time, let  $(x, z)$  be the Cartesian coordinates, let  $z^*(x, t)$  be the function describing the fluid interface locally, and let  $\rho_{h(l)}$ ,  $\mathbf{v}_{h(l)}$  and  $p_{h(l)}$  be the density, velocity and pressure of the heavy (light) fluid located in the region  $z > z^*$  ( $z < z^*$ ). The subscript  $h(l)$  marks the flow quantities of the heavy (light) fluid. The dynamics of incompressible immiscible fluids are governed by the following set of equations. In the bulk of the heavy (light) fluid,

$$\nabla \cdot \mathbf{v}_{h(l)} = 0, \quad \rho_{h(l)} \left( \frac{\partial \mathbf{v}_{h(l)}}{\partial t} + \mathbf{v}_{h(l)} \cdot \nabla \mathbf{v}_{h(l)} \right) + \nabla p_{h(l)} = 0. \quad (2.1)$$

The flow has no mass sources,

$$\mathbf{v}_h|_{z=+\infty} = \mathbf{v}_l|_{z=-\infty} = 0, \quad (2.2)$$

and the normal component of velocity  $\mathbf{v}_{n,h(l)}$  and pressure are continuous at the moving interface  $z^*(x, t)$ ,

$$\mathbf{v}_{n,h}|_{z=z^*} = \mathbf{v}_{n,l}|_{z=z^*}, \quad p_h|_{z=z^*} = p_l|_{z=z^*}. \quad (2.3a, b)$$

The length scale and time scale in the system (2.1), (2.2), (2.3) are defined by the initial conditions. The length scale  $\lambda$  is the period of the initial perturbation at the fluid interface in the  $x$  direction. The time scale is  $(\lambda/v_0)$ , where  $v_0$  is the initial growth rate. We assume that the  $x$  direction is normal to the initial shock, and the value of  $v_0$  is set by the shock-interface interaction in the linear regime of compressible RMI (Wouchuk 2001a). The incompressible inviscid problem (2.1), (2.2), (2.3) is ill-posed, and elementary methods for solving the problem are precluded owing to the singular aspects of the interface dynamics.

The nonlinear RM flow is characterized by the large-scale structure, small-scale structures, and energy transport between the large and small scales (Chebotareva *et al.* 1999; Collins & Jacobs 2002; Jacobs & Krivets 2005; Zabusky *et al.* 2003). The large-scale structure is coherent and this is an array of bubble and spikes, characterized by the period  $\lambda$  and the position  $h$  of the bubble or spike. The small-scale vortical structures are driven by shear, and their dynamics is in general non-deterministic (Frisch 1995), and is not defined uniquely by the initial conditions. According to observations (Chebotareva *et al.* 1999; Collins & Jacobs 2002; Jacobs & Krivets 2005), for fluids with contrasting densities the scales can be separated, and the large-scale coherent motion can be regarded as irrotational, with  $\nabla \times \mathbf{v}_{h(l)} = 0$ . The idea of separation in the RT/RM unstable flows of the large-scale structure, which is ‘passively advected’, from the active small-scale structures, was suggested first by Aref & Tryggvason (1989) and then developed by Abarzhi (2001) and Abarzhi *et al.*

(2003). The scale separation is applicable as long as the period of the coherent structure is invariable and the energy transport between the scales is not extensive.

The large-scale coherent dynamics adequately represents the nonlinear evolution of the bubble front in a vicinity of its tip, where the flow is potential. To describe this evolution, we reduce the governing equations (2.1), (2.2), (2.3) to a local dynamical system (Abarzhi 2001; Abarzhi *et al.* 2003). All calculations are performed in a non-inertial frame of reference moving with the velocity  $v(t)$  in the  $z$  direction, where  $v(t)$  is the bubble velocity and  $v = dh/dt$ . In the moving frame of references, the bubble tip is the point of stagnation, and the fluids experience effective acceleration  $-\partial v/\partial t$ . With  $\mathbf{v}_{h(t)} = \nabla\Phi_{h(t)}$ , we expand the potential(s)  $\Phi_{h(t)}$  as a Fourier series,

$$\Phi_h = \sum_{m=1}^{\infty} \Phi_m(t)(\cos(mkx) \exp(-mkz)/mk + z), \quad (2.4a)$$

$$\Phi_l = \sum_{m=1}^{\infty} \tilde{\Phi}_m(t)(\cos(mkx) \exp(mkz)/mk - z), \quad (2.4b)$$

where  $k = 2\pi/\lambda$  is the wave vector (wavenumber). The symmetry  $x \rightarrow -x$  imposed in the expansions (2.4) is required for global stability of the coherent structure under modulations with very large scales  $\gg \lambda$  (Abarzhi 2001; Abarzhi *et al.* 2003). For  $(x/\lambda) \sim 0$  the bubble front has the form  $z^*(x, t) = \sum_{i=0}^N \zeta_i(t)x^{2N}$ , where  $N$  is the order of approximation,  $\zeta_0(t) = 0$ , and  $\zeta_1(t) < 0$  is the principal curvature at the bubble tip. Substituting these expressions into the governing equations, taking the first integral of (2.1), and re-expanding the boundary conditions (2.2), (2.3) for  $(x/\lambda) \sim 0$ , we derive a system of ordinary differential equations for surface variables  $\zeta_i(t)$  and moments  $M_n(t) = \sum_{m=1}^{\infty} \Phi_m(t)(km)^n$  and  $\tilde{M}_n(t) = \sum_{m=1}^{\infty} \tilde{\Phi}_m(t)(km)^n$ , where  $n$  and  $m$  are integers.

In the zeroth order of approximation,  $N = 0$ , the bubble front has the form  $z^*(x, t) = 0$ , and the ‘no mass source’ condition (2.2) is reduced to

$$M_0 = -\tilde{M}_0 = -v, \quad (2.5)$$

whereas the equations (2.3a, b) have a trivial form,  $0 = 0$ . In the first order of approximation,  $N = 1$ , the bubble front has the form  $z^*(x, t) = \zeta_1(t)x^2$ , and the equations (2.3a, b) are reduced to

$$\dot{\zeta}_1 = 3\zeta_1 M_1 + M_2/2 = 3\zeta_1 \tilde{M}_1 - \tilde{M}_2/2, \quad (2.6a)$$

$$(\dot{M}_1/2 + \zeta_1 \dot{M}_0 - M_1^2/2 - \zeta_1) \rho_h = (\dot{\tilde{M}}_1/2 - \zeta_1 \dot{\tilde{M}}_0 - \tilde{M}_1^2/2 - \zeta_1) \rho_l. \quad (2.6b)$$

In the second order of approximation,  $N = 2$ , the interface is  $z^*(x, t) = \zeta_1(t)x^2 + \zeta_2(t)x^4$ , and the expansions (2.5), (2.6) of the conditions (2.3a, b) are further augmented with the equations

$$\begin{aligned} \dot{\zeta}_2 &= 5\zeta_2 M_1 - 5M_2 \zeta_1^2/2 - 5M_3 \zeta_1/3! - M_4/4! \\ &= 5\zeta_2 \tilde{M}_1 + 5\tilde{M}_2 \zeta_1^2/2 - 5\tilde{M}_3 \zeta_1/3! + \tilde{M}_4/4!, \end{aligned} \quad (2.7a)$$

$$\begin{aligned} \rho_h (\dot{M}_3/4! + \zeta_1 \dot{M}_2/2 + \dot{\zeta}_1 M_2/2 + \zeta_1 \dot{\zeta}_1 M_1 + \zeta_1^2 \dot{M}_1/2 - \zeta_2 \dot{M}_0 \\ + \zeta_1^2 M_1^2/2 - \zeta_1 M_1 M_2/2 - M_1 M_3/3! + M_2^2/8) \\ = \rho_l (\dot{\tilde{M}}_3/4! - \zeta_1 \dot{\tilde{M}}_2/2 - \dot{\zeta}_1 \tilde{M}_2/2 + \dot{\zeta}_1 \zeta_1 \tilde{M}_1 + \zeta_1^2 \dot{\tilde{M}}_1/2 + \zeta_2 \dot{\tilde{M}}_0 \\ + \zeta_1^2 \tilde{M}_1^2/2 + \zeta_1 \tilde{M}_1 \tilde{M}_2/2 - \tilde{M}_1 \tilde{M}_3/3! + \tilde{M}_2^2/8). \end{aligned} \quad (2.7b)$$

For  $N > 2$  the dynamical system is very cumbersome, and is not considered here. We emphasize that the ‘no mass source’ condition (2.2) is reduced to the equation

(2.5) in zeroth order of approximation,  $N = 0$ , and has no other expansion terms in higher orders,  $N \geq 1$ . We would like to point the attention of the reader to important symmetry property of equations (2.5)–(2.7), following from conditions (2.1)–(2.3) and expansion (2.4). Equations (2.5)–(2.7) remain invariant under transformation  $\rho_h \rightarrow \rho_l$  if odd moments and their time-derivatives change as  $M_{2n+1} \rightarrow \tilde{M}_{2n+1}$  and  $\dot{M}_{2n+1} \rightarrow \dot{\tilde{M}}_{2n+1}$ , and even moments and their time-derivatives change as  $M_{2n} \rightarrow -\tilde{M}_{2n}$  and  $\dot{M}_{2n} \rightarrow -\dot{\tilde{M}}_{2n}$ .

The system (2.5), (2.6), (2.7) describes the dynamics of the bubble front as long as the period of the coherent structure is invariable. The presentation in terms of moments allows one to account for the effect of higher-order spatial correlations. The dynamical system (2.5), (2.6), (2.7) cannot be integrated explicitly in time because of the closure problem. However, one can find the solution for the system in some limiting cases.

Initially,  $t(v_0/\lambda) \ll 1$ , the perturbation amplitude is small, the dynamics of the bubble front is described by the equations (2.5), (2.6) and only first-order harmonics are accounted for, that is,  $N \leq 1$ ,  $m = 1$  and  $M_2 = kM_1 = k^2M_0$  with  $\tilde{M}_2 = k\tilde{M}_1 = k^2\tilde{M}_0$ . For  $t(v_0/\lambda) \ll 1$ , the bubble velocity and curvature in (2.5), (2.6) change linearly with time, as  $\zeta_1 \sim -tv_0/\lambda^2$  and  $v - v_0 \sim -tv_0^2/\lambda$ . In the nonlinear regime, the perturbation amplitude is not small,  $N > 1$ , and the contribution of higher-order harmonics cannot be neglected. Asymptotically, for  $t(v_0/\lambda) \gg 1$ , the equations (2.5), (2.6), (2.7) have regular solutions, which can be represented as infinite time series. To the leading order in time, the velocity  $v$  and moments  $M_n, \tilde{M}_n$  approach zero with time as  $1/t$ , whereas the surface variables  $\zeta_i$  are time-independent.

To describe the nonlinear dynamics of the bubble front in a single-mode approximation, one considers the equations (2.5), (2.6) for  $N \leq 1$ , and retains only first-order harmonics in the expressions for the moments, i.e.  $N \leq 1$  and  $m = 1$ , with  $M_2 = kM_1 = k^2M_0$  and  $\tilde{M}_2 = k\tilde{M}_1 = k^2\tilde{M}_0$ . Then, the equations (2.5) and (2.6a, b) are reduced, respectively, to

$$M_0 = -\tilde{M}_0 = -v, \quad (2.8a)$$

$$\dot{\zeta}_1 = kM_0(3\zeta_1 + k/2) = k\tilde{M}_0(3\zeta_1 - k/2), \quad (2.8b)$$

$$(k\dot{M}_0/2 + \zeta_1\dot{M}_0 - k^2M_0^2/2 - \zeta_1)\rho_h = \rho_l(k\dot{\tilde{M}}_0/2 - \zeta_1\dot{\tilde{M}}_0 - k^2\tilde{M}_0^2/2 - \zeta_1). \quad (2.8c)$$

As is obvious from system (2.8), and as was pointed out first by Abarzhi (2001), in the nonlinear regime, the single-mode approximation does not satisfy simultaneously the two boundary conditions: the ‘no mass sources’ condition, (2.2), (2.5), (2.8a), and the condition of continuity of the normal component of velocity at the interface, (2.3a), (2.6a), (2.8b). To avoid this difficulty, Goncharov (2002) introduced an inhomogeneous time-dependent mass flow of the light fluid at the infinity, violated the boundary condition (2.2), (2.5), (2.8a), and found a single-mode solution with the curvature  $\zeta_1 = \zeta_D = -k/6$  and velocity  $v = v_D = (1 + A/3)/(1 + A)kt$ , and with  $A$  being the Atwood number  $A = (\rho_h - \rho_l)/(\rho_h + \rho_l)$ . Here the subscript  $D$  emphasizes that the solution  $(v_D, \zeta_D)$  agrees with the assumptions of the drag model of Oron *et al.* (2001). However, the drag model solution does not satisfy in the zeroth order of approximation the conservation of mass (2.2).

To obtain a regular asymptotic solution describing the nonlinear dynamics of the bubble front, we have to account for the higher-order correlations and the non-local properties of the flow that has singularities. The singularities determine the interplay of harmonics in the global flow as well as in the local dynamical system. They therefore influence the shape and velocity of the regular bubble. We account for this influence on the basis of symmetry arguments, that is, we consider all local

$N = 2, m = 3$	$ \Phi_{2,A}/\Phi_{1,A} $	$ \Phi_{3,A}/\Phi_{1,A} $	$ \tilde{\Phi}_{2,A}/\tilde{\Phi}_{1,A} $	$ \tilde{\Phi}_{3,A}/\tilde{\Phi}_{1,A} $	$v_{A,N=2}/v_{A,N=1}$
$A \approx 1$	$e^{-0.77}$	$e^{-2.34}$	$e^{-1.14}$	$e^{-3.47}$	$1 + e^{-1.77}$
$A \approx 0$	$e^{-0.91}$	$e^{-2.71}$	$e^{-0.91}$	$e^{-2.71}$	$1 + e^{-2.21}$

TABLE 1. The fastest solution in the family of regular asymptotic solutions.

asymptotic solutions allowed by the symmetry of the global flow. As in Abarzhi (2001) and Abarzhi *et al.* (2003), we assume that the bubble shape is free and is parametrized by the principal curvature at the bubble tip. In this way, we establish proper relations between the moments, solve the closure problem in (2.6), (2.7) and find a continuous one-parameter family of regular asymptotic solutions. Then we perform the stability analysis and choose the fastest stable solution in the family as the physically significant one.

To leading order in time,  $\zeta_1 = 0$  and, according to (2.6a), the bubble curvature is  $\zeta_1 = -M_2/6M_1 = \tilde{M}_2/6\tilde{M}_1$ . In the first approximation, we retain first- and second-order harmonics in the expressions for the moments, i.e.  $N = 1$  and  $m = 2$ , and obtain  $M_0 = \Phi_1 + \Phi_2 = (3M_1/2k)(1 - M_2/3M_1k)$  and  $\tilde{M}_0 = \tilde{\Phi}_1 + \tilde{\Phi}_2 = (3\tilde{M}_1/2k)(1 - \tilde{M}_2/3\tilde{M}_1k)$  with  $v = -M_0 = \tilde{M}_0$ . Then the bubble velocity is  $v = -(3M_1/2k)(1 + 2\zeta_1/k)$ , and the ratio  $M_1/\tilde{M}_1 = -(1 - 2\zeta_1/k)/(1 + 2\zeta_1/k)$ . In this way, we derive from equations (2.5), (2.6) the bubble velocity as a function of the bubble curvature and the Atwood number:

$$v = \frac{3}{2kt} \frac{(1 + A(\zeta_1/k) - 12A(\zeta_1/k)^3)}{(A - 4(\zeta_1/k) + 4A(\zeta_1/k)^2)} (1 - 4(\zeta_1/k)^2). \tag{2.9}$$

The bubble is concave down,  $\zeta_1 < 0$ , and for solutions in the family (2.9) the velocity  $v$  is a regular function on  $\zeta_1$ . In the interval  $\zeta_{cr} < \zeta_1 \leq 0$  the interplay of harmonics is well captured and the lowest-order harmonics are dominant:

$$\left. \begin{aligned} \Phi_1 &= \frac{2}{kt} \frac{(1 - 2(\zeta_1/k))(1 + 3(\zeta_1/k))}{(A - 4(\zeta_1/k) + 4A(\zeta_1/k)^2)} (-1 - A(\zeta_1/k) + 12A(\zeta_1/k)^3), \\ \tilde{\Phi}_1 &= \frac{2}{kt} \frac{(1 + 2(\zeta_1/k))(-1 + 3(\zeta_1/k))}{(A - 4(\zeta_1/k) + 4A(\zeta_1/k)^2)} (-1 - A(\zeta_1/k) + 12A(\zeta_1/k)^3), \\ \Phi_2 &= -v - \Phi_1, \quad \tilde{\Phi}_2 = v - \tilde{\Phi}_1. \end{aligned} \right\} \tag{2.10}$$

As is seen from (2.10) for  $\zeta_1 \approx \zeta_{cr}$  the convergence is broken, as the magnitudes of higher-order amplitudes become compatible with the magnitudes of the lower-order amplitudes, as in Abarzhi (2002) in the case of  $A = 1$ . For  $A \sim 1$  the value of  $\zeta_{cr} \approx -k/4$ , and for  $A \sim 0$  it is  $\zeta_{cr} \approx 0$ . The fastest solution in the family (2.9), (2.10) is the solution with the curvature  $\zeta_1 = \zeta_A = 0$  and velocity  $v = v_A = 3/2Akt$ . As  $t(v_0/\lambda) \rightarrow \infty$  the velocity  $v_A \rightarrow 0$ . Here the subscript  $A$  emphasizes that the solution  $(v_A, \zeta_A)$  is obtained for the Atwood number  $A \leq 1$ .

In second-order approximation in space,  $N = 2$ , we retain the first-, second-, and third-order harmonics in the expressions for the moments,  $M_n(t) = \sum_{m=1}^3 \Phi_m(t)(km)^n$  and  $\tilde{M}_n(t) = \sum_{m=1}^3 \tilde{\Phi}_m(t)(km)^n$ , and obtain the one-parameter family of regular asymptotic solutions similarly to (2.9), (2.10). The family is cumbersome and is not presented here. For the fastest solution with  $\zeta_1 = \zeta_A = 0$ , and the values of the amplitudes and velocity are given in table 1. In higher approximation,  $N > 2$ , for solutions in the family, the Fourier amplitudes decay with increase in their number, and the higher-order corrections are small.

To analyse stability of the solutions thus obtained, we derive the higher-order corrections in the asymptotic time series expansion. For every  $N$ , we slightly perturb  $\zeta_i \rightarrow \zeta_i + \theta_i$ ,  $M_n \rightarrow M_n + \mu_n$ ,  $\tilde{M}_n \rightarrow \tilde{M}_n + \tilde{\mu}_n$ , linearize the equations (2.5), (2.6), (2.7) in terms of small  $\theta_i$ ,  $\mu_n$  and  $\tilde{\mu}_n$ , and derive the values of  $\theta_i \sim t^{-b_i}$  and  $\mu_n, \tilde{\mu}_n \sim t^{-1-b_i}$ . The exponents  $b_i$  are the complex functions dependent on the Atwood number and the bubble curvature,  $b_i = b_i(A, \zeta_1)$ . For stable solutions, the real part of the exponents should be positive  $\text{Re}(b_i) > 0$ . This criterion yields that in the one-parameter family (2.9) the solutions with  $\zeta_1 \sim 0$  are stable, whereas solutions with finite curvatures  $\zeta_1 \sim \zeta_{cr}$  are unstable. Therefore, the physically significant solution in the RM family corresponds to a decelerating bubble flattened at the tip:

$$tv_0/\lambda \rightarrow \infty, \quad \zeta_1 \rightarrow \zeta_A, \quad v \rightarrow v_A, \quad \zeta_A = 0, \quad v_A = 0, \quad (2.11)$$

with  $v_A = C/Akt$  and  $C \sim 2$ , so that  $v_A \sim \lambda/A\pi t$ .

At first glance, the fact that the flattened bubble in the family (2.9) moves faster than the bubble with a finite curvature seems to contradict the everyday experience. This controversy is, however, apparent. Indeed, as the bubble velocity decays with time as  $v \sim F/kt$ , the magnitude of the bubble deceleration  $|dv/dt|$  is  $\sim F/t^2$ . Thus, the larger the value of  $F$ , the faster the bubble moves, and the stronger are its deceleration and drag. The bubble with a flattened surface experiences more drag and has a larger deceleration magnitude than that with a finite curvature. This, in turn, implies that the coefficient  $F$  in the velocity  $v \sim F/kt$  has to be larger for a flattened bubble compared the case of a bubble with a finite curvature, in agreement with our results (2.9).

As  $v_A t/\lambda \sim 1/A$ , then for fluids with close densities,  $0 < A \ll 1$ , the bubbles move faster and decelerate more strongly compared the case of fluids with highly contrasting densities with  $A \approx 1$ . For finite  $t$ , the velocity  $v_A t/\lambda \rightarrow \infty$  as  $A \rightarrow 0$ . This indicates that for fluids with similar densities the velocity of the nonlinear RM bubble may have a time-dependence faster than  $1/t$ , such as  $t^a$  with  $-1 < a < 0$ , and the exponent in this power law decay may depend on the Atwood number. It is worth mentioning that the time-dependence of the previous non-local solution is derived under the assumption that, in the RM flow, one can separate the small-scale vortical structures from the passively advecting large-scale structure. For fluids with close densities,  $A \sim 0$ , the size of the vortical structures which appear on the sides of the evolving spikes, is large and is comparable with the period of the coherent structure. Therefore, for  $A \sim 0$ , the scale separation may not work and the potential theory may be inapplicable.

The above analysis suggests the following evolution of the bubble front in the Richtmyer–Meshkov instability. The shock-interface interaction results in a growth of the small perturbation at the fluid interface (Richtmyer 1960). As the coherent structure appears, the bubble velocity decreases, its shape becomes more curved, and these changes are linear with time. In the weakly nonlinear regime, the bubble curvature reaches an extreme value, dependent on the initial conditions and the Atwood number. Asymptotically, the bubble flattens,  $\zeta \rightarrow 0$ , and decelerates,  $v \rightarrow 0$ . The flattening of the bubble front is a distinct feature of RMI and it follows from the fact that the velocity of RM bubbles decays as a power law with time. For fluids with similar densities,  $0 < A \ll 1$ , the nonlinear bubbles move faster compared to the case of  $A \approx 1$ .

According to our theory, in the highly nonlinear regime of RMI the velocity of the bubble front is represented by the infinite time series  $v \sim C/Akt(1 + \sum_{j=1}^{\infty} B_j(tk v_0)^{-b_j} + \text{c.c.})$ , where the integer  $j$  denotes the order of correction and c.c. denotes the complex conjugate. The values of  $b_j$  are derived via the stability analysis, and the coefficients  $B_j$  are free parameters, dependent on the initial conditions. As found earlier,



$N = 1, \zeta = 0$	$A = 0.9$	$A = 0.78$	$A = 0.663$	$A = 0.55$
$b_1$	$-2.11 - 0.86i$	$-2.28 - 1.07i$	$-2.51 - 1.33i$	$-2.82 - 1.68i$

TABLE 2. The exponents of the next-order term in the velocity time-series.

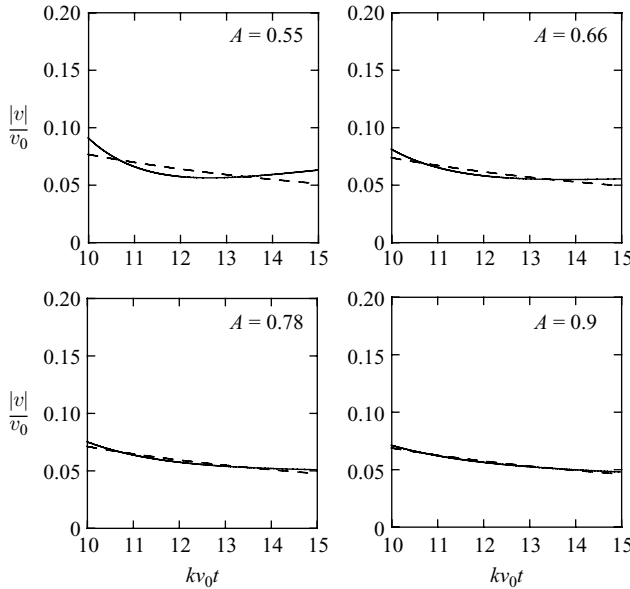


FIGURE 1. Velocity of the nonlinear RM bubble given by the non-local theory accounting for the next-order correction in time (solid) and the single-scale drag model (dashed).

$0 < \text{Re}(b_1) < \text{Re}(b_2) < \dots < \text{Re}(b_i)$ , so the solution (2.11) remains stable. However, the stability of the solution (2.11) is asymptotic but not exponential (Korn & Korn 1968). The higher-order corrections are power laws, which decay slowly and do not have characteristic time scale of the decay. This implies that, asymptotically, as  $tkv_0 \rightarrow \infty$ , the bubble velocity approaches  $v \rightarrow F_A/kt$ , where  $F_A = C/A$ , but for a finite time  $tkv_0 \gg 1$ , the contribution of terms  $\sim |F_A B_j v_0 (tkv_0)^{-1-b_j}|$  may be comparable to that of the term  $F_A/kt$ . For a finite sequence of data points and a short dynamic range in observation time in the experimental and simulation data sets, a reliable quantification of the exponent  $-1$  and the coefficient  $F_A$  of the asymptotic velocity  $v_A$  can be very difficult.

This challenge is illustrated by figure 1, showing the bubble velocity given by the drag model  $v_D = (1 + A/3)/(1 + A)kt$  and by our solution,  $v = 3/2Akt + v_0 B_1 (tv_0 k)^{-b_1} + \text{c.c.}$ , which describes the asymptotic dynamics of a flattened bubble in first approximation,  $N = 1$ , and accounts for the next-order correction in time. The exponent  $b_1$  is given by the stability analysis (see table 2), and the coefficient  $B_1$  is chosen to provide the best fit to the drag model solution in the time interval  $10 < tv_0 k < 15$ . This time interval ensures the nonlinearity of the dynamics and it is wider compared to the time intervals used for a quantification of the nonlinear dynamics in the experiments and simulations (Youngs 1994; Collins & Jacobs 2002; Robey *et al.* 2003; Glendinning *et al.* 2003; Miles *et al.* 2004; Jacobs & Krivets 2005). Four different values of the Atwood number are considered with  $0 \ll A < 1$ . An excellent, within  $\sim 10\%$ , ‘fit’ of the two solutions in figure 1 illustrates

that, based solely on the velocity data, one can hardly distinguish between the results of the single-scale drag model, which violates the conservation laws, and our non-local theory, which accounts for the higher-order corrections in space and time and identifies the essentially multiscale character of the interface dynamics.

### 3. Simulations

To simulate the evolution of the two-dimensional Richtmyer–Meshkov instability, we solve the compressible Navier–Stokes equations,

$$\frac{\partial \rho}{\partial t} + \nabla \cdot (\rho \mathbf{v}) = 0, \quad (3.1a)$$

$$\frac{\partial \rho \mathbf{v}}{\partial t} + \nabla \cdot (\rho \mathbf{v} \mathbf{v}) + \nabla p + \nabla \cdot \boldsymbol{\tau} = 0, \quad (3.1b)$$

$$\frac{\partial \rho E}{\partial t} + \nabla \cdot ([\rho E + p] \mathbf{v}) + \nabla \cdot \mathbf{q} + \boldsymbol{\tau} : \nabla \mathbf{v} = 0, \quad (3.1c)$$

where  $\rho$  and  $\mathbf{v}$  are the fluid density and velocity respectively,  $p$  is the pressure,  $\mathbf{q}$  is the heat flux

$$\mathbf{q} = -\Lambda \nabla T, \quad (3.2)$$

where  $T$  is the temperature and  $\Lambda$  is the thermal conductivity. The stress tensor  $\boldsymbol{\tau}$  is

$$\boldsymbol{\tau} = -\mu [(\nabla \mathbf{v}) + (\nabla \mathbf{v})^T] + \frac{2}{3} \mu (\nabla \cdot \mathbf{v}) \mathbf{I}, \quad (3.3)$$

where  $\mu$  is the dynamic viscosity and  $\mathbf{I}$  is the unity tensor. The total energy  $E$  is

$$E = \frac{p/\rho}{\gamma - 1} + \frac{1}{2} \mathbf{v}^2, \quad (3.4)$$

and for both fluids the ratio of the specific heats is  $\gamma = 1.4$ . The dynamic viscosity is calculated using the Sutherland formula,

$$\mu = \mu_{ref} (T/T_{ref})^{3/2} \frac{T_{ref} + S_1}{T + S_1}, \quad (3.5)$$

with  $\mu_{ref}$  being the reference viscosity and  $S_1 = 110$  K. The thermal conductivity  $\Lambda$  is determined using a Prandtl number of  $Pr = 0.76$ . The fluids are ideal gases with the equation of state

$$p = \rho \Phi T, \quad (3.6)$$

where  $\Phi$  is the gas constant of either the light or heavy fluid. In our simulations, the flow has no mass sources and there is neither mass flux across nor slip at the moving interface. Therefore, the normal and tangential components of velocity, as well as the pressure and temperature, are continuous at the fluid interface. The density jump at the interface is caused by the change in the gas constant  $\Phi$ .

The fluid interface  $\Gamma$  is located at  $z^*(x, t)$  and is tracked by a level set scalar  $G$ . With  $\mathbf{x} = (x, z)$ , we define

$$G(\mathbf{x}, t)|_{\Gamma} = G_0 = \text{const.}, \quad (3.7)$$

where  $G(\mathbf{x}, t) < G_0$  in the light fluid and  $G(\mathbf{x}, t) > G_0$  in the heavy fluid. Then the evolution equation for the scalar  $G$  can be derived by differentiation of equation (3.7) in time,

$$\frac{\partial G}{\partial t} + \mathbf{v} \cdot \nabla G = 0. \quad (3.8)$$

This equation is called the level set equation (Osher & Sethian 1988). It is independent of the choice of  $G$  away from the interface. However, to facilitate the numerical solution of (3.8),  $G$  is chosen as a distance function away from the interface,

$$|\nabla G|_{G \neq G_0} = 1. \tag{3.9}$$

### 3.1. Numerical method

In our numerical simulations, the Navier–Stokes equations (3.1) are solved using a second-order space and time accurate hybrid capturing/tracking scheme, originally proposed by Smiljanovski, Moser & Klein (1997) for deflagration waves. In modelling the evolution of RMI, the scheme ensures that the location and dynamics of the interface are tracked explicitly by the level set equation, while the shocks and expansion fans are treated by a standard capturing scheme. The main advantage of this approach is that the simplicity and robustness of the standard capturing schemes are retained, whereas the interfacial processes are described with an accuracy comparable to standard tracking schemes. The hybrid capturing/tracking scheme has no unphysical numerical fluxes across the interface. The interface remains a density discontinuity for all times, even for very large values of the Atwood number.

To solve the level set equations (3.8) and (3.9), we use a standard fifth-order WENO scheme for Hamilton–Jacobi equations (Jiang & Peng 2000), and employ a PDE-based iterative scheme for equation (3.9) (Sussman, Smereka & Osher 1994; Peng *et al.* 1999). The following two subsections summarize briefly the hybrid capturing/tracking scheme (Smiljanovski *et al.* 1997; Schmidt & Klein 2003) and its modification for RMI simulation.

#### 3.1.1. In-cell reconstruction

In finite volume schemes, the cell value of a conserved quantity  $U^{i,j}$  is defined as the volume average of the quantity,

$$U^{i,j} = \frac{1}{V^{i,j}} \int_{V^{i,j}} U(\mathbf{x}') d\mathbf{x}', \tag{3.10}$$

averaged over the cell volume  $V^{i,j}$ . Assuming within each cell a piecewise constant distributions of  $U$  for the light and heavy fluid, we reduce expression (3.10) to

$$U^{i,j} = \alpha U_h^{i,j} + (1 - \alpha) U_l^{i,j}, \tag{3.11}$$

where  $\alpha$  is the fraction of the cell volume of the heavy fluid,

$$\alpha = \frac{1}{V^{i,j}} \int_{V^{i,j}} H(G(\mathbf{x}') - G_0) d\mathbf{x}', \tag{3.12}$$

and  $H$  is the Heaviside function.

For the in-cell reconstruction scheme, the key idea is to use only  $U_h^{i,j}$  and  $U_l^{i,j}$  instead of  $U^{i,j}$  to compute the face fluxes in cells, which contain a part of the interface. We reconstruct  $U_h^{i,j}$  and  $U_l^{i,j}$  from  $U^{i,j}$  using a combination of the jump conditions of  $U$  across the interface,

$$\mathbf{v}_h|_{G=G_0} = \mathbf{v}_l|_{G=G_0}, \quad p_h|_{G=G_0} = p_l|_{G=G_0}, \quad T_h|_{G=G_0} = T_l|_{G=G_0} \tag{3.13a, b, c}$$

with equations (3.11) and (3.12).

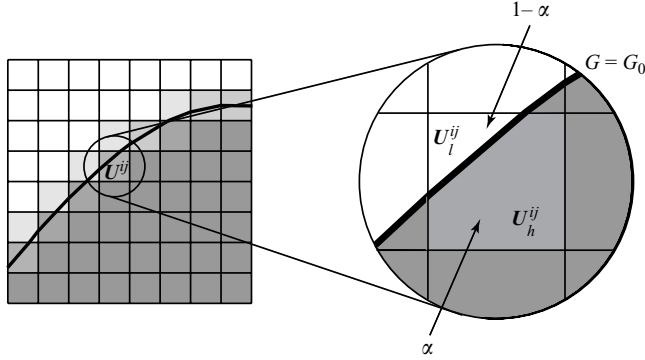


FIGURE 2. In-cell reconstruction.

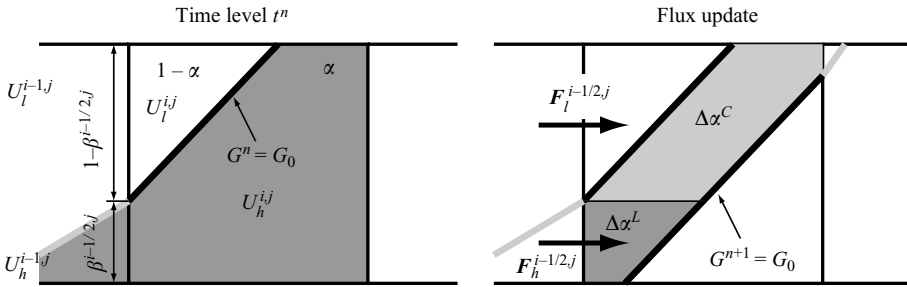


FIGURE 3. Flux update in cells containing part of the interface.

### 3.1.2. Cell update

An operator splitting technique (Strang 1967) is employed to advance the numerical solution in time. In order to obtain the correct update, all gradients in the individual operator steps must be calculated using only cell values of the same fluid type.

For the diffusion operator, the gradients are computed using a second-order central difference scheme. The corresponding stencils across the interface therefore involve the reconstructed cell values  $U_h$  and  $U_l$ , plus one additional adjacent cell value on the opposite side of the interface. This cell first has to be transformed into the corresponding matching state using the jump conditions at the interface, before the gradients are evaluated. In this operation, our method resembles the ghost fluid approach (Fedkiw *et al.* 1999).

In the convection operator, we solve the cell face Riemann problems using a second-order wave distribution algorithm (LeVeque 1990), and formally recast the individual wave contributions in the form of cell face fluxes  $F^{i-1/2,j}$  and  $F^{i+1/2,j}$ . However, special care must be taken if a cell  $(i, j)$  contains part of the interface at  $t^n$  or  $t^{n+1}$ , as shown in figure 3. To ensure the correct computation of the flux, the individual cell face fluxes for both the heavy,  $F_h^{i-1/2,j}$ , and the light fluid,  $F_l^{i-1/2,j}$ , are calculated using only (reconstructed) quantities of the relevant fluid. Then, the average cell face flux  $F^{i-1/2,j}$  is

$$F^{i-1/2,j} = \beta^{i-1/2,j} F_h^{i-1/2,j} + (1 - \beta^{i-1/2,j}) F_l^{i-1/2,j}, \quad (3.14)$$

with  $\beta$  being the heavy fluid cell face fraction: see figure 3. Note that, because our convection operator is based on a wave distribution scheme,  $F^{i-1/2,j}$  takes into

account only those wave contributions that arise from the cell face Riemann problem. Since the interface itself constitutes a separate wave, its contribution to the change of  $U^{i,j}$  must be accounted for additionally as

$$\Delta U^{i,j} = \Delta\alpha^C (U_h^{i,j} - U_l^{i,j}) + \Delta\alpha^L (U_h^{i-1,j} - U_l^{i-1,j}) + \Delta\alpha^R (U_h^{i+1,j} - U_l^{i+1,j}). \quad (3.15)$$

Here,  $\Delta\alpha^C$  is the change of the heavy fluid cell volume fraction due to the motion of the interface within the cell  $(i, j)$  itself, and  $\Delta\alpha^L$  and  $\Delta\alpha^R$  are the contributions due to movement from adjacent cells to the left, respectively right: see figure 3. Note that (3.15) implies that the global conservation property of the numerical scheme is now dependent on the accuracy of  $\Delta\alpha$ , and therefore relies on the accuracy of the level set method.

Finally, a combination of (3.14) and (3.15) yields the update for  $U^{i,j}$  in cells with part of the interface:

$$\begin{aligned} U^{n+1,i,j} = & U^{n,i,j} + \frac{\Delta t}{\Delta x} \{ (\beta^{i-1/2,j} F_h^{i-1/2,j} + (1 - \beta^{i-1/2,j}) F_l^{i-1/2,j}) \\ & - (\beta^{i+1/2,j} F_h^{i+1/2,j} + (1 - \beta^{i+1/2,j}) F_l^{i+1/2,j}) \\ & + \Delta\alpha^C (U_h^{i,j} - U_l^{i,j}) + \Delta\alpha^L (U_h^{i-1,j} - U_l^{i-1,j}) \\ & + \Delta\alpha^R (U_h^{i+1,j} - U_l^{i+1,j}) \}. \end{aligned} \quad (3.16)$$

One of the major advantages of equation (3.16) is that the Courant–Friedrichs–Lewy (CFL) condition can be based on the grid size  $\Delta x$  of the underlying grid, as the cell updates are performed on the basis of cell-volume-averaged quantities only.

## 4. Results

In this section we outline the computational setup, verify and validate our numerical method, discuss the diagnostics of the interface dynamics, and compare the simulation results with the theory and the models.

### 4.1. Computational setup

We study numerically the evolution of RMI for a weak initial shock with Mach number  $Ma = 1.2$ , which propagates from the light to heavy fluid, and for four different Atwood numbers  $A = 0.55$ ,  $A = 0.663$ ,  $A = 0.78$ , and  $A = 0.9$ . The computational domain is  $[-40.667\lambda, 1.333\lambda] \times [-0.5\lambda, 0.5\lambda]$  and it is resolved by  $5376 \times 128$  equidistant Cartesian grid cells. In the  $z$  direction, outflow boundary conditions are employed at the external boundaries of the computational domain. In the  $x$  direction, we use symmetry conditions and calculate only one half of the wavelength. Initially, the interface is located at  $z = 0$  and it is slightly perturbed with a sinusoidal disturbance  $z^*(x, t = 0) = a_0 \cos(kx)$ , where the perturbation wavelength is  $\lambda = 2\pi/k = 3.75$  cm and the initial pre-shock amplitude is  $a_0 = a(t = 0) = 0.064\lambda$  (Benjamin, Besnard & Haas 1993).

If the interface were ideally planar, it would move with a characteristic post-shock velocity  $v_\infty$ . The velocity  $v_\infty$  depends on the Atwood number, the shock strength, and the speed of sound  $c$ . The value of  $v_\infty$  can be obtained from one-dimensional calculations (Meshkov 1969). With the Mach number and the speed of sound fixed, the value of  $v_\infty$  is smaller for higher Atwood number  $A$ . In our simulations  $v_\infty = 0.219c_l$  for  $A = 0.55$ ,  $v_\infty = 0.195c_l$  for  $A = 0.663$ ,  $v_\infty = 0.163c_l$  for  $A = 0.78$ , and  $v_\infty = 0.117c_l$  for  $A = 0.9$ , and  $c_l = 347.2 \text{ m s}^{-1}$ .

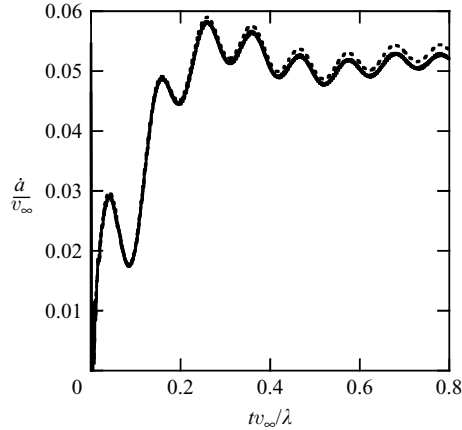


FIGURE 4. Growth rate  $\dot{a}$  in the linear regime of RMI, for  $A=0.9$  and  $Ma=1.2$ . The solid line is the numerical simulation, the dashed line is the solution given by the linear theory of Wouchuk (2001a).

In all simulations the time step is given by a constant CFL number of 0.8. Note that the simulations are performed for the viscous Navier–Stokes equations, and the dynamic viscosity  $\mu$  is the same in the heavy and light fluids, with  $Re = \rho_l v_\infty \lambda / \mu_{ref} = 13042$  ( $A=0.55$ ),  $Re = 11572$  ( $A=0.663$ ),  $Re = 9700$  ( $A=0.78$ ), and  $Re = 6968$  ( $A=0.9$ ). The influence of viscosity is small, and this allows one to compare the simulations with the inviscid theories. To verify the statement, we performed a series of test runs based solely on the Euler equations, and found that the influence of viscosity is indeed insignificant. The negligible effect of viscosity can be related to the choice of the symmetry boundary conditions in the  $x$  direction. Under these conditions, boundary layers, which may influence the instability evolution, do not appear on the boundaries of the computational domain.

#### 4.2. Verification and validation of the numerical method

To verify and validate the applicability of our numerical method for modelling RMI dynamics, we perform two test runs, and compare the growth of the instability in the simulations with that given by the compressible linear theory and by the experiment. In the simulations, the positions of the bubble and spike and therefore the perturbation amplitude  $a$  are calculated from the bilinear interpolation of the level set scalar  $G$  along  $x=0$  and  $x=\lambda/2$ . Then, the amplitude growth rate  $\dot{a}$  is determined from the velocity field  $\mathbf{v}$ , conditioned on the location of the bubble and the spike tips,  $\dot{a} = ((\mathbf{v} \cdot \mathbf{n})|_s - (\mathbf{v} \cdot \mathbf{n})|_b)/2$ , where  $\mathbf{n} = \nabla G / |\nabla G|$  is the normal vector of the fluid interface.

In the former verification test, we compare our numerical results with the linear theory of Wouchuk (2001a). This theory captures the baroclinic production of vorticity caused by the shock-interface interaction and, in contrast to linear impulsive models (Richtmyer 1960; Meyer & Blewett 1972; Vandenboomgaerde *et al.* 1998), provides an adequate value of the RMI growth rate for fluids with highly contrasting densities. Figure 4 compares the growth rate of the amplitude  $\dot{a}$  obtained in the simulations with that derived by Wouchuk (2001a) for  $A=0.9$ . For early times, when the nonlinear effects are negligible, the agreement between the linear theory of Wouchuk (2001a) and the simulation is excellent. The growth rate of the linear RMI in this case is  $v_0 \approx 0.055 v_\infty = 2.23 \text{ m s}^{-1}$ . Figure 4 shows that the growth rate of the amplitude

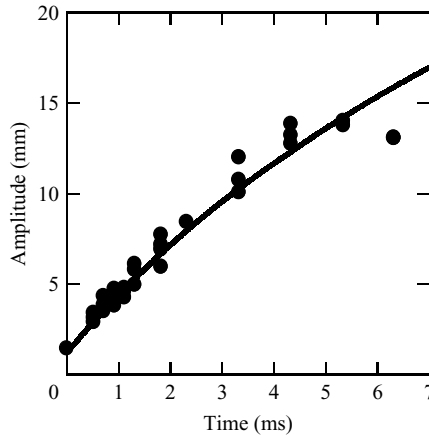


FIGURE 5. Amplitude versus time for  $A=0.663$  and  $Ma=1.1$ . The solid line is the numerical simulation, the symbols are experimental results taken from Jones & Jacobs (1997).

exhibits oscillations caused by the reverberations of sound waves. Predicted first by the linear theory of Wouchuk (2001*a*), these oscillations are accurately reproduced in our simulations. As is seen from figure 4, the amplitude of the oscillations is about 10–20% of the initial growth rate, whose value is on the order of 5% of the velocity  $v_\infty$ , which is, in turn, about 10% of the speed of sound  $c_l$ . The amplitude of the oscillations is therefore very small compared to the speed of sound, and the oscillations do not induce significant pressure fluctuations. However, due to the oscillations, the peak of  $\dot{a}$  is about 10% higher than the growth rate of the RMI in the linear regime.

In the latter validation case, we compare our simulations with the experiments of Jones & Jacobs (1997). Figure 5 shows the evolution of the perturbation amplitude. For the experiments and the simulation run presented in figure 5, a shock with Mach number  $Ma=1.1$  hits a cosinusoidally perturbed interface with wavelength  $\lambda=5.9333$  cm and initial amplitude  $a_0=0.15$  cm. The Atwood number in this case is  $A=0.663$ , and all other initial and boundary conditions are those described in §4.1. As is seen from figure 5, the growth of the perturbation amplitude obtained in the simulations agrees with the experimental data (Jones & Jacobs 1997). We emphasize that in figure 5 the velocity oscillations are also present and can be derived from our numerical solution as the time-derivative of the amplitude. However, the experiments of Jones & Jacobs (1997) do not capture the oscillations, as the data set in figure 5 is a collage of single-shot measurements of a series of different experiments. Overall, the agreement between the simulations and the linear theory, figure 4, as well as the experiment, figure 5, is excellent. Our results suggest that for a reliable diagnostics of the small oscillations and the initial growth rate in the experiments, in addition to continuous visualization and high temporal and spatial resolutions, the values of the Mach number and the Atwood number should be controlled with a relative accuracy of at least  $10^{-3}$ – $10^{-4}$ , which is an extremely challenging task.

#### 4.3. Diagnostics of the nonlinear dynamics

Figure 6 depicts the nonlinear evolution of the Richtmyer–Meshkov instability for  $A=0.55$ ,  $A=0.663$ ,  $A=0.78$ , and  $A=0.9$ . Our simulations stop as the reflected shock hits the interface. In figure 6, the bubbles are located in the centre, the spikes are on the sides, and the roll-up of vortices forms mushroom-shaped spikes. In the case

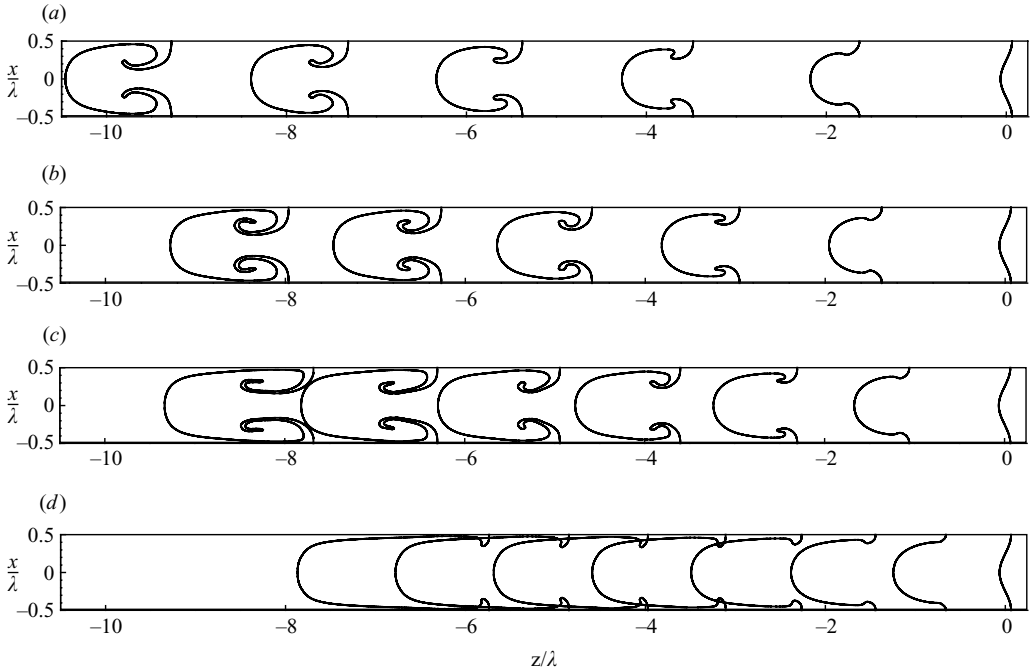


FIGURE 6. Evolution of the fluid interface for (a)  $A=0.55$ , (b)  $A=0.663$ , (c)  $A=0.78$ , and (d)  $A=0.9$ , every 1 ms starting at  $t=0$  ms.

of fluids with highly contrasting densities,  $A=0.9$ , the roll-up of vortices is less pronounced, in agreement with the observations (Youngs 1994; Collins & Jacobs 2002; Robey *et al.* 2003; Glendinning *et al.* 2003; Miles *et al.* 2004; Jacobs & Krivets 2005). The employed grid resolution might be insufficient to grasp all small-scale structures in the roll-up regions. It is sufficient, however, to describe adequately the large-scale coherent dynamics and to capture the evolution of the bubble front in the vicinity of its tip.

To quantify the evolution of the Richtmyer–Meshkov instability, we first define the length scale and time scale of the flow. The length scale is the period of the coherent structure  $\lambda$ . To perform a comparative study of various stages of RMI (linear, weakly and highly nonlinear), most existing observations use the time scale set by the initial growth rate  $v_0$  as  $\lambda/v_0$  (Youngs 1994; Collins & Jacobs 2002; Robey *et al.* 2003; Glendinning *et al.* 2003; Miles *et al.* 2004; Jacobs & Krivets 2005). However, as discussed earlier, figures 4 and 5, the experiments do not capture the interface dynamics in detail. The reverberations of sound waves, appearing in the linear regime of RMI, can add uncontrolled contributions to the measured value of  $v_0$  and can therefore make the value of the time scale inaccurate. To avoid this difficulty, we choose the time scale set by the velocity  $v_\infty$  at which an ideally planar interface would move after the shock passage. The velocity  $v_\infty$  can be obtained directly from one-dimensional calculations (Meshkov 1969). The choice of the time scale as  $\lambda/v_\infty$  allows one to make the diagnostics repeatable and more reliable.

To study the nonlinear dynamics of RMI, we use two diagnostic parameters, the bubble velocity and the bubble curvature. The bubble velocity is a traditional diagnostic parameter. In many existing observations of RMI, the velocity of the bubble front is determined relative to a ‘middle line’: half the distance between the



tips of the bubble and spike, i.e. one half of the amplitude  $a/2$ . This kind of data analysis may result in significant inaccuracies, especially in the nonlinear regime of RMI, when the bubbles and spikes are not symmetric. To determine the bubble velocity more accurately, we account for the fact that RMI develops relative to a background motion with the constant velocity  $v_\infty$ . Therefore, the  $z$ -coordinate of the reference point is  $v_\infty t$ , and in the laboratory frame of reference the bubble velocity is  $(v + v_\infty)$ , whereas in the frame of references moving with velocity  $v_\infty$ , the bubble velocity is  $v$ .

The curvature of the bubble front can be calculated via two distinct approaches. In the first approach, one can compute the curvature from the level set scalar as  $\kappa = 2\zeta = \nabla \cdot \mathbf{n} = \nabla \cdot (\nabla G / |\nabla G|)$ . This computation limits the evaluation of the curvature value to the symmetry point, i.e. the very tip of the bubble, and is thus extremely sensitive to small-scale fluctuations. To obtain the large-scale dynamics of the bubble front from the simulation data, we apply another approach (Oparin & Abarzhi 1999). First, from the level set scalar field, we calculate via bilinear interpolation the positions of the interface  $z_i^*$  at different locations  $|x_i| \leq x_\zeta$  for some given  $x_\zeta$ , spaced a constant grid size  $\Delta x$  apart. Then we compute the curvature  $\zeta$  using a least-squares fit of a circle with radius  $R = 1/2\zeta$  to the discrete locations  $(x_i, z_i^*)$  of the interface. This approach effectively ‘removes’ the small-scale fluctuations of the bubble curvature and retains only its large-scale behaviour, captured by the nonlinear theory. If the shape of the interface is not ideally circular, the numerical value of the bubble curvature can be a function of  $x_\zeta$ . This is illustrated by figure 7, which depicts the temporal evolution of the bubble curvature for different values of  $x_\zeta$ . For  $A = 0.55$ , the shape of the bubble front is very close to that of an ever-expanding circle. As the Atwood number increases, the inner region of the nonlinear bubble becomes nearly flat, followed by a sharp transition into the spike region: see figure 6. With an increase in  $x_\zeta$  the value of  $\zeta$  slightly increases. We emphasize, however, that to estimate the performance of our nonlinear theory and the single-scale drag models (Goncharov 2002; Oron *et al.* 2001; Alon *et al.* 1995), for a given moment of time, the exact numerical value of  $\zeta$  is not necessary to obtain. Only the asymptotic value and the trend of  $\zeta(t)$  for  $t \rightarrow \infty$  is important, as the difference between the values of  $\zeta_A = 0$  and  $\zeta_D = -\pi/3$  is large enough to differentiate.

#### 4.4. Comparison of numerical results to the nonlinear theory and models

Figure 8 shows the evolution of the bubble velocity  $v(t)$  in the frame of reference moving with velocity  $v_\infty$  for all four Atwood number cases. As is seen from figure 8, the bubble is accelerated ‘impulsively’ by a passing shock, and in the linear regime its velocity reaches a maximum value. As the coherent structure appears, the bubble decelerates. The bubble velocity decreases linearly with time in the weakly nonlinear regime, and approaches zero asymptotically, in agreement with the foregoing analysis. The velocity evolution is accompanied by oscillations, caused by the reverberations of the sound waves. The oscillations occur in the linear regime of the instability (figure 4), and are damped with time only slightly as the fluids are nearly inviscid (figure 8).

Several PADE and heuristic models described the evolution of the bubble front for ‘all times’, from the linear to the highly nonlinear regime of RMI (Zhang & Sohn 1997; Oron *et al.* 2001). The predictive capability of these (well-calibrated) models should be extensively tested, as the models heavily use adjustable parameters to compare with the experimental data, and are therefore biased (Hastie, Tibshirani & Friedman 2001). The nonlinear evolution of RMI is accompanied by finite-time

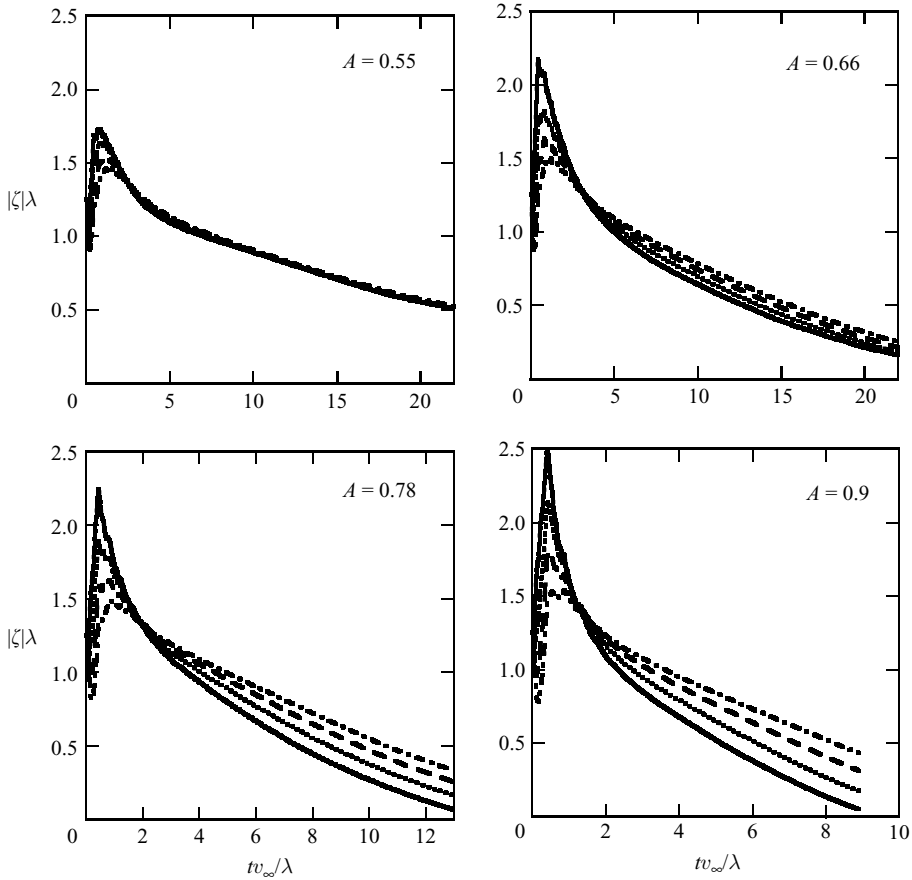


FIGURE 7. Bubble curvature  $\zeta(t)$  evaluated for  $x_\zeta = 4/64\lambda$  (solid line),  $x_\zeta = 6/64\lambda$  (dotted line),  $x_\zeta = 8/64\lambda$  (dashed line), and  $x_\zeta = 10/64\lambda$  (dash-dotted line).

singularities, which occur at small scales and are sensitive to the density ratio and the initial conditions and whose dynamics is a fundamental and unresolved problem, such that to date none of the existing theories provide a rigorous description of the evolution of the entire interface in RMI for ‘all times’ (for details see Velikovich 1996; Wouchuk 2001a; Abarzhi 2002; Matsuoka *et al.* 2003; Abarzhi *et al.* 2003; and references therein). Our theoretical analysis considers only the large-scale coherent dynamics and reports the regular asymptotic solutions describing the dynamics of the bubble front in the vicinity of its tip. We derive the asymptotic nonlinear solutions to leading order in time, account for the higher-order correlations in space, and find the next-order corrections in the time series expansion.

The properties of our non-local solution differ substantially from those of the single-mode models (Oron *et al.* 2001; Goncharov 2002). According to our results, for RM flow without mass sources, the dynamics of the nonlinear bubble is described by the infinite power law time series, and the higher-order spatial correlations significantly affect the values of the diagnostic parameters. The nonlinear RM bubble decelerates and flattens, and to leading order in time  $v_A = F_A/kt$ , where  $F_A = C/A$ , and  $\zeta_A = 0$ . The shape of the bubble front is not determined solely by the spatial period of the coherent structure  $\lambda$  and is therefore influenced by the longitudinal scale  $h$ .

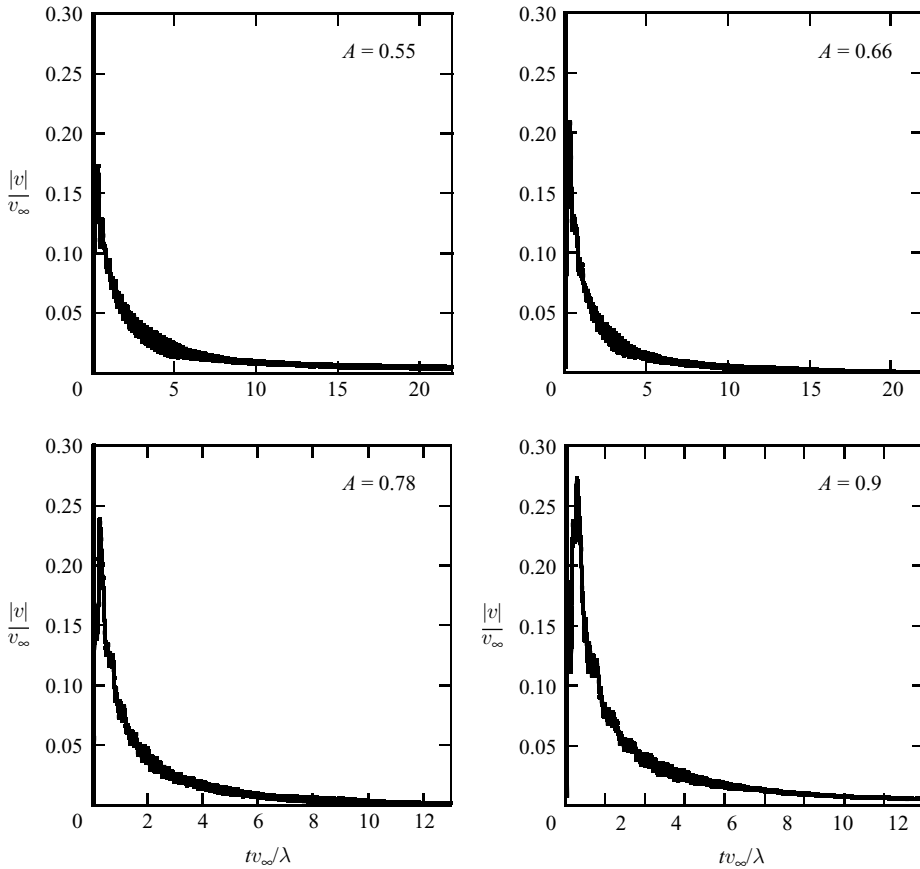


FIGURE 8. Bubble velocity as a function of time.

The single-scale models (Oron *et al.* 2001; Goncharov 2002) suggest that the bubble velocity is a rational function of time, and to leading order in time the velocity of the nonlinear bubble decays as  $v_D = F_D/kt$ , where  $F_D = (1 + A/3)/(1 + A)$ , whereas its curvature is finite and density-ratio-independent and is set uniquely by the period  $\lambda$  as  $\zeta_D = -\pi/3\lambda$ . The single-scale solution can be derived from the conservation laws only if the flow has an inhomogeneous time-dependent mass source (Goncharov 2002). For a given value of the Atwood number, the fast flattened bubble with  $(v_A, \zeta_A)$  decelerates more strongly and experiences more drag compared to the slow curved bubble with  $(v_D, \zeta_D)$ .

At first glance, as the ratio  $v_A/v_D$  is large, one could distinguish between the solutions via a comparison with the bubble velocity in observations. In the experiments, however, one commonly measures the bubble position  $h$  (Aleshin *et al.* 1988, 1990; Collins & Jacobs 2002; Glendinning *et al.* 2003; Robey *et al.* 2003; Jacobs & Krivets 2005). For  $v_A$  and  $v_D$ , the bubble displacement is  $h \sim (F_{A(D)}/k) \log(t/\tau)$ . The logarithmic corrections to power laws (as in the nonlinear RMI) are comparable with the experimental errors and are ill-defined (see, for instance, Gol'din *et al.* 1973). Using Taylor series expansions, one can readily ascertain that log-dependence can be approximated by power law dependence with small, slightly varying exponents. A log correction to a power law can be confused with

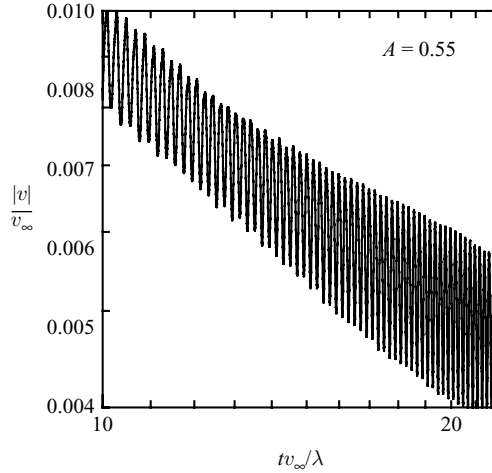


FIGURE 9. Log-log plot of the bubble velocity  $v(t)$  in the nonlinear regime.

small corrections for the exponent of the power law itself (Gol'din *et al.* 1973). The coefficient  $F_{A(D)}$  of the logarithmic dependence is therefore extremely sensitive to the manner of data truncation and is impossible to evaluate accurately for a finite sequence of data points and a short dynamic range in the observation time.

In our simulations, the bubble velocity  $v$  can be measured directly, and with the scaling  $v_\infty$ , the numerical results can be analysed more accurately compared to other observations. Still, based solely on the velocity data (figures 1 and 8), we cannot distinguish between the results of our non-local theory (2.11) and the single-mode models (Oron *et al.* 2001; Goncharov 2002). As the asymptotic velocity of the bubble front is represented by a power law time series, a large dynamic range is required for accurate quantification of the exponent and the pre-factor of the leading-order term in the series (Gol'din *et al.* 1973). For a finite sequence of data points and a short dynamic range, an excellent fit between the two solutions can be easily obtained (as in figure 1). Yet, unless several (at least two or three) decades of scales in the observation time are considered, the exponent and pre-factor of the power law cannot be estimated accurately. In fluid dynamics, intense quantitative studies of power law dependences have been performed, for instance in homogeneous isotropic turbulence (Sreenivasan 1999) and turbulent convection (Grossmann & Lohse 2000). In isotropic homogeneous turbulence, two to three decades of scales are the accepted level of standards for the estimate of power law exponents in turbulent energy spectra (see Sreenivasan 1999 and references therein). In turbulent convection, to evaluate the scaling exponent of the Nusselt number with the Rayleigh number, as many as nine decades of the Rayleigh number have been considered (Grossmann & Lohse 2000).

Another complexity in the quantification of the nonlinear dynamics in the Richtmyer–Meshkov instability originates from flow compressibility. As is seen from figure 8, in the nonlinear regime of compressible RMI, the evolution of the bubble velocity is accompanied by oscillations. These oscillations appear in the linear regime of the instability and are induced by the reverberations of the sound waves, (figure 4). In the nonlinear regime, the bubble velocity decreases, whereas the amplitude of the oscillations is damped only slightly. Figure 9 presents the log-log plot of the bubble velocity versus time in the nonlinear regime of RMI for the case  $A = 0.55$ . This density ratio is close to that in the experiments of Jacobs & Krivets (2005), whereas the time

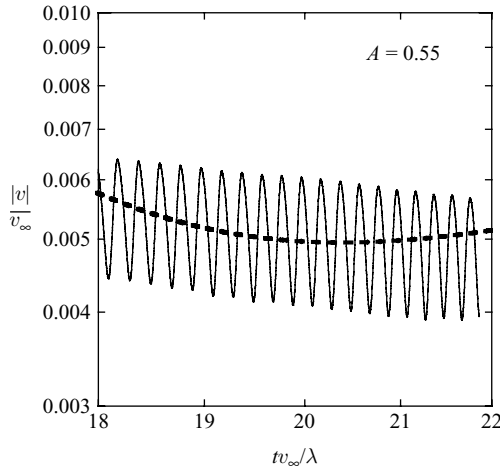


FIGURE 10. Log-log plot of the bubble velocity  $v(t)$  in the nonlinear regime given by the simulations (solid) and by the non-local theory for  $N = 1$ , and accounted for the next-order correction in time (dashed).

considered is significantly longer. Figure 9 illustrates that the quantification of the time-dependence of the bubble velocity from the simulation data is a real challenge.

Figure 10 shows the fit of the bubble velocity in the simulations by our nonlinear solution with  $v = 3/2Akt + v_0 B_1 (tv_0 k)^{-b_1} + \text{c.c.}$  which describes the bubble front dynamics in first approximation in space,  $N = 1$ , and accounts for the first-order correction in the time series expansion in the case  $A = 0.55$ . The value of  $b_1$  is given in table 2 and  $v_0/v_\infty = 0.178$ . The left bound of the time interval in figure 10 is chosen to ensure the nonlinearity of the dynamics, and it is  $\sim 3\lambda/v_0$ , whereas the right bound is the time when the simulation stops, and it is significantly longer than that in the experiments of Jacobs & Krivets (2005). The curve fit is excellent, but the short dynamic range in  $t$  prevents us from making a quantitative evaluation of the time-dependence of the bubble velocity. On the basis of our observations we can state only that the nonlinear RM bubble decelerates with time (figure 8) and its velocity approaches zero asymptotically (figure 9).

We see that the measurement of the bubble curvature has a crucial importance for clarifying the issue of whether the nonlinear dynamics of RMI is a single-scale or a multiscale process. If indeed it were a single-scale process, then the spatial period  $\lambda$  would uniquely define the shape of the bubble front and asymptotically  $|\zeta| \approx 1/\lambda$ , as suggested by the drag and single-mode models (Oron *et al.* 2001; Goncharov 2002). Figure 11 shows the evolution of the bubble curvature  $\zeta(t)$  for all four Atwood number cases. As is seen from figure 11, after the shock passage, the bubble front is becoming curved. The bubble curvature changes linearly with time and reaches an extreme value in the weakly nonlinear regime. Then its absolute value decreases and approaches zero. Figure 11 also presents the root-mean-square deviation  $\zeta'$  of the curvature  $\zeta$  evaluated at  $x_\zeta = 4/64\lambda$  for all four cases. In each case, the root-mean-square deviation is small, ensuring that the curvature of the bubble front is calculated accurately.

The evolution of the bubble curvature from the simulations confirms the results of the non-local theory (2.11) and disagrees with the solution  $\zeta_D = -k/6 \approx -1.05/\lambda$  given by the single-scale models. According to our results, the shape of the bubble

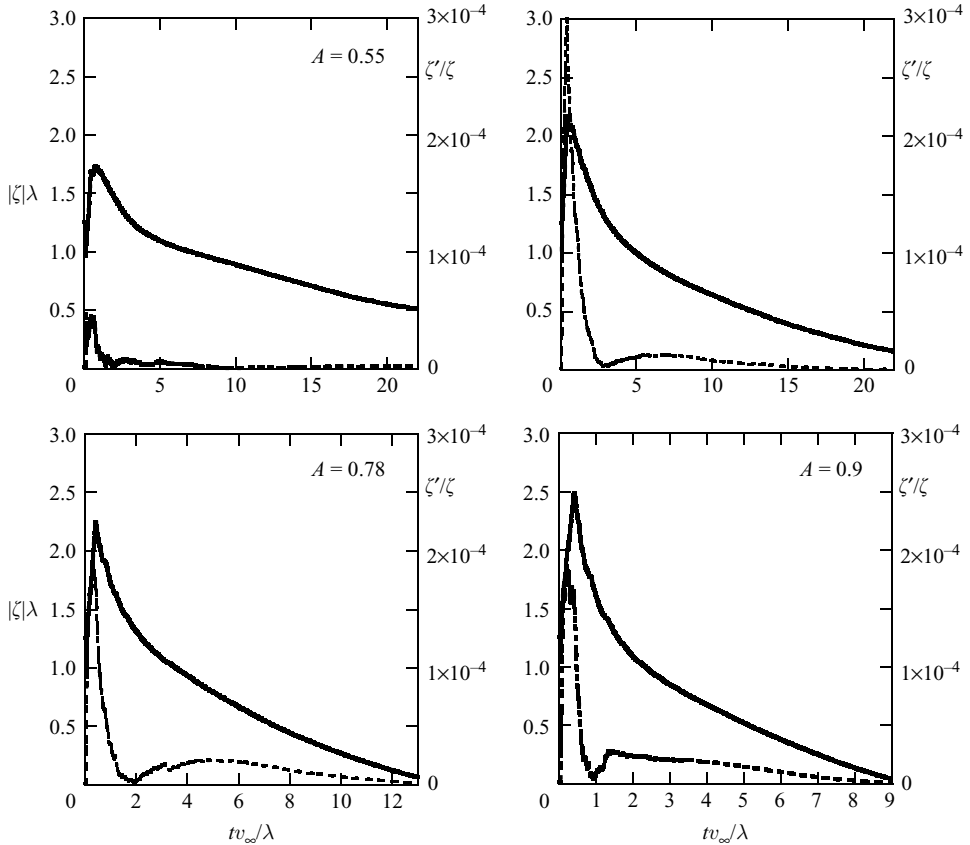


FIGURE 11. Bubble curvature  $\zeta(t)$  for  $x_\zeta = 4/64\lambda$  and its r.m.s. deviation. In each case the solid line is  $\zeta$  with the scale on the left, and the dashed line is  $\zeta'/\zeta$  with the scale on the right.

front in RMI is not determined solely by the spatial period  $\lambda$ . It is therefore sensitive to the longitudinal scale  $h$ . For fluids with high and intermediate contrasting densities,  $A=0.663$ ,  $A=0.78$ , and  $A=0.9$ , the decay in the curvature value is clearly visible from figure 11, and for smaller Atwood numbers it takes longer for the bubble to flatten. In the case of  $A=0.55$  the flattening process is significantly slower than for the other three cases. For  $A=0.55$ , at a time when the reflected shock hits the interface and our simulations stop, the absolute value of the bubble curvature remains finite,  $|\zeta| = 0.516/\lambda$ , yet this is already twofold smaller than  $|\zeta_D|$  (Oron *et al.* 2001; Goncharov 2002). We emphasize that the flattening of the bubble front remains in the Euler simulations, and is observed in the experiments of Collins & Jacobs (2002), Glendinning *et al.* (2003), and Jacobs & Krivets (2005). As discussed earlier, the single-mode solution  $(v_D, \zeta_D)$  has a time-dependent inhomogeneous mass source. Therefore, the curvature of the bubble front is the relevant and sensitive diagnostic parameter, whose value tests whether the normal component of velocity is continuous at the fluid interface, and whether the flow has no artificial mass sources.

To conclude this section, we review the comparison between the experiments performed by Jacobs & Krivets (2005), the single-scale model (Oron *et al.* 2001; Goncharov 2002), and our theory. Our theory suggests the following diagnostic parameters: the mass source, the bubble velocity and the curvature of the bubble front.

The experiments of Jacobs & Krivets (2005) have no mass sources, report deceleration and flattening of the bubble front, and mention that for fluids with similar densities the RM bubbles move faster than in the case of fluids with contrasting densities. Therefore, qualitatively, these experiments confirm our theoretical predictions, not the conclusions of the single-mode drag model. On the other hand, Jacobs & Krivets (2005) report a quantitative agreement of the experimental data with the value of the bubble velocity  $v_D$  predicted by the single-mode models, which is significantly lower than the leading-order term in the velocity expansion  $v_A$  found by our theory. As discussed earlier, this agreement is not surprising, as in the experiments of Jacobs & Krivets (2005) the *overall* observation time is short,  $\leq 10/kv_0$  and is limited to approximately one decade in scales, the value of the initial growth rate is not a direct measurement, and the experimental data points are a collage of single-shot measurements of a series of different experiments. *De facto*, the experiments of Jacobs & Krivets (2005) may apply the results of the single-mode models to calibrate the experimental value of the initial growth rate (which varies from one data point to another), rather than to estimate the exponent (not to say pre-factor) of the leading-order term in the asymptotic velocity expansion. The data calibration is a very important and necessary step in the evaluation of quality of experimental data sets, but it may be insufficient for an adequate quantitative description of the nonlinear dynamics of such a complex phenomenon as the Richtmyer–Meshkov instability.

## 5. Discussion and conclusion

We performed a systematic study of the nonlinear evolution of the Richtmyer–Meshkov instability. The flow is two-dimensional, the shock is weak and passes from the light to the heavy fluid, the amplitude of the initial perturbation is small, and the fluids have highly contrasting densities as well as an intermediate density ratio. The large-scale coherent dynamics is considered, and the evolution of the bubble front is diagnosed. RMI develops relative to a background motion with a constant velocity  $v_\infty$ , at which the interface would move if it were ideally planar. The obtained analytical and numerical results are summarized in the phase diagram in figure 12, representing the bubble velocity  $v(t)$  versus bubble curvature  $\zeta(t)$ , with time  $t$  being a parameter. Initially the bubble exhibits an abrupt acceleration caused by the shock-interface interaction (Richtmyer 1960; Meshkov 1969). Then the bubble starts to decelerate, while the absolute value of the bubble curvature increases and reaches an extreme value. We emphasize that the bubble velocity and curvature reach their extreme values at two distinct moments of time. As the instability evolves, the bubble continues to decelerate and its curvature approaches zero, as found by the non-local theory. Our numerical and analytical results agree with one another and show that for fluids with similar densities the bubbles move faster and flatten more slowly than those for fluids with highly contrasting densities. Our analysis indicates that the exponent of the power law decay of the velocity of the nonlinear RM bubble may depend on the Atwood number (Abarzhi 2001; Abarzhi *et al.* 2003). It is worth mentioning that in figure 12 the magnitude of  $|v|/v_\infty$  is larger for higher Atwood numbers because the value of  $v_\infty$  is smaller for higher Atwood numbers (compare, for instance, figure 6). In our simulations, the incident shock propagates from the light to heavy fluid; however, the flattening of the bubble front may also be observed in the ‘heavy-to-light’ configuration. We shall address a detailed numerical study of this case in the future.

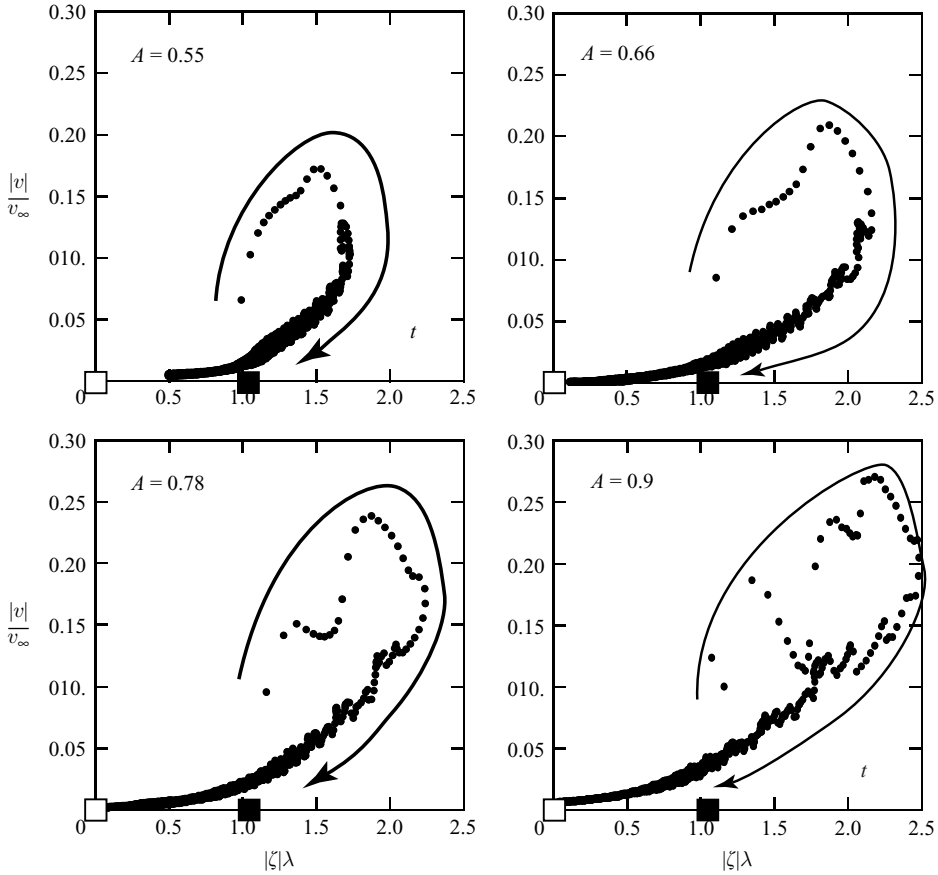


FIGURE 12. Bubble velocity  $v(t)$  as function of the bubble curvature  $\zeta(t)$ , with time  $t$  being a parameter. Black circles are samples of the numerical solution roughly every  $\Delta t v_\infty/\lambda = 0.0196$  for  $A = 0.55$ ,  $\Delta t v_\infty/\lambda = 0.0173$  for  $A = 0.663$ ,  $\Delta t v_\infty/\lambda = 0.0146$  for  $A = 0.78$ , and  $\Delta t v_\infty/\lambda = 0.0104$  for  $A = 0.9$ . The white square is the asymptotic solution given by the non-local theory, the black square corresponds to the single-mode and drag models.

In many of the existing observations, the nonlinear dynamics is quantified as follows (Youngs 1994; Collins & Jacobs 2002; Glendinning *et al.* 2003; Jacobs & Krivets 2005). The characteristic time scale is set by the value of the initial growth rate  $v_0$ , which is hard to measure accurately. The only diagnostic parameter is the bubble (spike) position, calculated with respect to the ‘middle line’, one half of the amplitude. The data sampling does not have high temporal resolution, the dynamic range of the overall observation time is short (approximately one decade), the Mach and Atwood numbers are controlled coarsely, and the velocity oscillations caused by sound waves are either not captured (experiments) or disregarded (simulations). As discussed earlier, this type of analysis of the observation data may contain significant inaccuracies. To quantify our simulations of the nonlinear RMI, we apply another diagnostics. We set the time scale using the velocity  $v_\infty$ , at which the interface would move if it were ideally planar. The bubble velocity and curvature are both monitored. The bubble (spike) position is calculated in the frame of reference moving with velocity  $v_\infty$ . The data sampling has a high-frequency temporal component, and the oscillations of the velocity, caused by the reverberations of sound waves, are



captured. The time interval considered in our simulations is significantly longer than in other observations. However, in the nonlinear regime of RMI, we can evaluate only asymptotic values of the diagnostic parameters, as the accurate quantitative estimate of their time-dependences is prevented due to the velocity oscillations and the relatively short dynamic range of the simulation time.

Our simulations confirm the qualitative effect predicted and explained by our non-local theory: flattening of the bubble front in the nonlinear regime of RMI. Our results do not confirm predictions of the single-scale models (Alon *et al.* 1995; Oron *et al.* 2001; Goncharov 2002). We show that these models explicitly violate the conservation laws. The heavy use of adjustable parameters, low temporal resolution and short dynamic range can explain the (apparent) agreement between the models and the observations. There is nothing wrong in a ‘curve fit’ of experimental data with adjustable parameters, but the range of applicability of such an approach and its predictive capability should not be overestimated (Gol’din *et al.* 1973). The excellent “curve fit” implies only that the drag models can be calibrated, and the observations of Youngs (1994), Collins & Jacobs (2002), Glendinning *et al.* (2003) and Jacobs & Krivets (2005) are consistent with one another. It does not, however, mean that the model captures correctly the essentials of the nonlinear dynamics. The large number of adjustable parameters induces bias (Hastie *et al.* 2001), which may, in fact, obscure the underlying physics of the phenomena, and may also lead to a false sense of agreement between the model and the experiments rather than providing grounds and directions for improvement in the information capacity and fidelity of the experimental data sets. According to our theoretical and numerical results, to build the solid grounds for understanding the turbulent mixing induced by the Richtmyer–Meshkov instability, existing experiments and simulations have to be augmented with highly resolved measurements of the velocity and density fields, lasting over a much longer dynamic range in the observation time, with a tight control over the experimental parameters, such as the Mach and Atwood numbers. These are tremendous experimental and numerical tasks, and they have not been solved so far.

Our results show that the flattening of the bubble front is a distinct property of the nonlinear evolution of the Richtmyer–Meshkov instability (compared, for instance, to RTI, as discussed by Abarzhi 2001 and Abarzhi *et al.* 2003). The flattening is not just an indication that, in the observations, the normal component of velocity is continuous at the fluid interface and the flow has no artificial mass sources. It shows that the nonlinear dynamics in RMI is a multiscale process, governed by two macroscopic length scales: the spatial period of the structure  $\lambda$  and the longitudinal scale  $h$ , which is the bubble (spike) displacement, i.e. the wavelength and the amplitude of the front. As illustrated by figure 12, in the nonlinear RMI the velocity of the bubble front  $v = (dh/dt)$  and its curvature  $\zeta$  mutually depend on one another:  $dh/dt = v_\infty f(|\zeta \lambda|)$ , where  $f$  is an algebraic function, and the processes of deceleration,  $d^2h/dt^2$ , and flattening,  $d(\zeta \lambda)/dt$ , are inter-related. Hence, to obtain a reliable description of the mixing process, it is essential to take account of the multiscale character of RMI dynamics.

To summarize, we have considered theoretically and numerically the large-scale coherent dynamics in the Richtmyer–Meshkov flow for fluids with high and intermediate density contrasts and for a small-amplitude initial perturbation in two dimensions. Our theory derives the asymptotic solutions to leading order in time, identifies the exponents of the next-order terms in the timeseries expansion, and accounts for the higher-order correlations in space. The theoretical solution has no adjustable parameters, indicates that the flattening of the bubble front is a distinct

property of RMI, and explains the nature of the phenomenon. Our simulations model the interface dynamics for compressible, immiscible, and nearly inviscid fluids. The numerical method treats the interface as a discontinuity and is applicable for fluids with very high values of the density ratio. Our simulations have high temporal resolution, run for a time significantly longer than in other observations, and monitor both the velocity and curvature of the bubble front. The theory and the simulations agree with one another. According to the results obtained, the evolution of RMI is a non-local and multiscale process, and the nonlinear RM bubbles flatten and decelerate. Our consideration indicates that the accuracy, resolution, and the dynamic range of the time of observation in the existing experiments may be insufficient for a rigorous quantification of the time-dependence of the nonlinear RMI. Further improvement of the interface diagnostics is required. The RMI phenomenon still remains a formidable task, open for a curious mind.

The authors thank Dr E. E. Meshkov for fruitful discussions, and Drs A. L. Velikovich, K. Nishihara, H. Robey, B. Remington, J. W. Jacobs, V. Krivets, A. Bershadskii, S. S. Orlov and K. R. Sreenivasan for valuable comments. We are very grateful to Dr G. Wouchuk for valuable consultations and for providing the results of the linear theory for comparison. The work has been supported financially by the US Department of Energy within the ASC program and by the Naval Research Laboratory.

#### REFERENCES

- ABARZHI, S. I. 2001 Nonlinear asymptotic solutions for RT and RM problems for fluids with finite density contrast. In *Proc. 8th Intl Workshop on the Physics of Compressible Turbulent Mixing*, p. 104. Pasadena, CA, USA.
- ABARZHI, S. I. 2002 Nonlinear evolution of unstable fluid interface. *Phys. Rev. E* **66**, 036301.
- ABARZHI, S. I., NISHIHARA, K. & GLIMM, J. 2003 Rayleigh–Taylor and Richtmyer–Meshkov instabilities for fluids with a finite density ratio. *Phys. Lett. A* **317**, 470–476.
- ALESHIN, A. N., GANALII, E. G. & ZAITSEV, S. G. 1988 Study of nonlinear and transition stages of the development of the Richtmyer–Meshkov instability. *Prisma V. Zh. Tekh. Fiziki* **14**, 1063–1067.
- ALESHIN, A. N., LAZAREVA, E. & ZAITSEV, S. G. 1990 A study of linear, nonlinear, and transition stages of Richtmyer–Meshkov instability. *Dokl. Akad. Nauk SSSR* **310**, 1105–1108.
- ALON, U., HECHT, J., OFFER, D. & SHVARTS, D. 1995 Power laws and similarity of Rayleigh–Taylor and Richtmyer–Meshkov mixing fronts at all density ratios. *Phys. Rev. Lett.* **74**, 534–537.
- AREF, H. & TRYGGVASON, G. 1989 Model of Rayleigh–Taylor instability. *Phys. Rev. Lett.* **62**, 749–752.
- BENJAMIN, R., BESNARD, D. & HAAS, J. 1993 Shock and reshock of an unstable interface. *LANL Rep. LA-UR 92-1185*, Los Alamos National Laboratory.
- CHEBOTAREVA, E. I., ALESHIN, A. N., ZAYTSEV, S. G. & SERGEEV, S. V. 1999 Investigation of interaction between reflected shocks and growing perturbation on an interface. *Shock Waves* **9**, 81–86.
- COLLINS, B. D. & JACOBS, J. W. 2002 PLIF flow visualization and measurements of the Richtmyer–Meshkov instability. *J. Fluid Mech.* **464**, 113–136.
- DIMONTE, G. 2000 Spanwise homogeneous buoyancy-drag model for Rayleigh–Taylor mixing and experimental evaluation. *Phys. Plasmas* **7**, 2255–2269.
- FEDKIW, R., ASLAM, T., MERRIMAN, B. & OSHER, S. 1999 A non-oscillatory Eulerian approach to interfaces in multimaterial flows (the ghost fluid method). *J. Comput. Phys.* **152**, 457–492.
- FRISCH, U. 1995 *Turbulence*. Cambridge University Press.
- GLENDINNING, S. G., BOLSTAD, J., BRAUN, D. G., EDWARDS, M. J., HSING, W. W., LASINSKI, B. F., LOUIS, H., MILES, A., MORENO, J., PEYSER, T. A., REMINGTON, B. A., ROBey, H. F., TURANO, E. J., VERDON, C. P. & ZHOU, Y. 2003 Effect of shock proximity on Richtmyer–Meshkov growth. *Phys. Plasmas* **10**, 1931–1936.

- GOL'DIN, L. L., IGOSHIN, F. F., KOZEL, S. M., KOLACHEVSKIJ, N. N., MAZAN'KO, I. P., NOGINOVA, L. V., RADKEVICH, I. A., ROGOZINSKIJ, K. A. & SAMARSKIJ, Y. A. 1973 *Rukovodstvo k Laboratornym Zanyatiyam po Fizike (Laboratories in General Physics)*, 2nd edn. Nauka.
- GONCHAROV, V. N. 2002 Analytical model of nonlinear, single-mode, classical Rayleigh–Taylor instability at arbitrary Atwood numbers. *Phys. Rev. Lett.* **88**, 134502.
- GROSSMANN, S. & LOHSE, D. 2000 Scaling in thermal convection: A unifying theory. *J. Fluid Mech.* **407**, 27–56.
- HASTIE, T., TIBSHIRANI, R. & FRIEDMAN, J. 2001 *The Elements of Statistical Learning*. Springer.
- HOLMES, R. L., DIMONTE, G., FRYXELL, B., GITTINGS, M. L., GROVE, J. W., SCHNEIDER, M., SHARP, D. H., VELIKOVITCH, A. L., WEAVER, R. P. & ZHANG, Q. 1999 Richtmyer–Meshkov instability growth: Experiment, simulation and theory. *J. Fluid Mech.* **389**, 55–79.
- JACOBS, J. W. & KRIVETS, V. V. 2005 Experiments on the late-time development of single-mode Richtmyer–Meshkov instability. *Phys. Fluids* **17**, (034105).
- JACOBS, J. & SHEELEY, J. 1996 Experimental study of incompressible Richtmyer–Meshkov instability. *Phys. Fluids* **8**, 405–415.
- JIANG, G.-S. & PENG, D. 2000 Weighted ENO schemes for Hamilton–Jacobi equations. *SIAM J. Sci. Comput.* **21**, 2126–2143.
- JONES, M. A. & JACOBS, J. W. 1997 A membraneless experiment for the study of Richtmyer–Meshkov instability of a shock-accelerated gas interface. *Phys. Fluids* **9**, 3078–3085.
- KORN, G. A. & KORN, T. M. 1968 *Mathematical Handbook for Scientists and Engineers: Definitions, Theorems and Formulas for Reference and Review*, 2nd edn. McGraw-Hill.
- KULL, F. 1991 Theory of Rayleigh–Taylor instability. *Phys. Rep.* **206**, 197.
- LEVEQUE, R. J. 1990 *Numerical Methods for Conservation Laws*. Birkhäuser.
- MATSUOKA, C., NISHIHARA, K. & FUKUDA, Y. 2003 Nonlinear evolution of an interface in the Richtmyer–Meshkov instability. *Phys. Rev. E* **67**, (036301).
- MESHKOV, E. 1969 Instability of the interface of two gases accelerated by a shock wave. *Sov. Fluid Dyn.* **4**, 101–104.
- MEYER, K. A. & BLEWETT, P. J. 1972 Numerical investigation of the stability of a shock-accelerated interface between two fluids. *Phys. Fluids* **15**, 753–759.
- MILES, A. R., EDWARDS, M. J., BLUE, B., HANSEN, J. F., ROBNEY, H. F., DRAKE, R. P., KURANZ, C. & LEIBRANDT, D. R. 2004 The effect of a short-wavelength mode on the evolution of a long-wavelength perturbation driven by a strong blast wave. *Phys. Plasmas* **11**, 5507–5519.
- OPARIN, A. & ABARZHI, S. 1999 Three-dimensional bubbles in Rayleigh–Taylor instability. *Phys. Fluids* **11**, 3306–3311.
- ORON, D., ALON, U., OFFER, D. & SHVARTS, D. 2001 Dimensionality dependence of the Rayleigh–Taylor and Richtmyer–Meshkov instability late-time scaling laws. *Phys. Plasmas* **8**, 2883–2889.
- OSHER, S. & SETHIAN, J. A. 1988 Fronts propagating with curvature-dependent speed: Algorithms based on Hamilton–Jacobi formulations. *J. Comput. Phys.* **79**, 12–49.
- PENG, D., MERRIMAN, B., OSHER, S., ZHAO, H. & KANG, M. 1999 A PDE-based fast local level set method. *J. Comput. Phys.* **155**, 410–438.
- RICHTMYER, R. 1960 Taylor instability in shock acceleration of compressible fluids. *Comm. Pure Appl. Maths.* **13**, 297.
- ROBNEY, H. F., ZHOU, Y., BUCKINGHAM, A. C., KEITER, P., REMINGTON, B. A. & DRAKE, R. P. 2003 The time scale for the transition to turbulence in a high Reynolds number, accelerated flow. *Phys. Plasmas* **10**, 614–622.
- SCHMIDT, H. & KLEIN, R. 2003 A generalized level-set/in-cell-reconstruction approach for accelerating turbulent premixed flames. *Combust. Theory Modelling* **7**, 243–267.
- SCHNEIDER, M., DIMONTE, G. & REMINGTON, B. 1998 Large and small scale structure in Rayleigh–Taylor mixing. *Phys. Rev. Lett.* **80**, 3507–3510.
- SHARP, D. H. 1984 An overview of Rayleigh–Taylor instability *Physica D* **12**, 3–15.
- SMILJANOVSKI, V., MOSER, V. & KLEIN, R. 1997 A capturing–tracking hybrid scheme for deflagration discontinuities. *Combust. Theory Modelling* **1**, 183–215.
- SREENIVASAN, K. R. 1999 Fluid turbulence. *Rev. Mod. Phys.* **71**, S383–S395.
- STRANG, G. 1967 On the construction and comparison of difference schemes. *SIAM J. Numer. Anal.* **5**, 506–517.

- SUSSMAN, M., SMEREKA, P. & OSHER, S. 1994 A level set method for computing solutions to incompressible two-phase flow. *J. Comput. Phys.* **114**, 146.
- VANDENBOOMGAERDE, M., MUEGLER, C. & GAUTHIER, S. 1998 Impulsive model for the Richtmyer–Meshkov instability. *Phys. Rev. E* **58**, 1874–1882.
- VELIKOVICH, A. L. 1996 Analytic theory of Richtmyer–Meshkov instability for the case of reflected rarefaction wave. *Phys. Fluids* **8**, 1666–1679.
- WOUCHUK, J. 2001*a* Growth rate of the linear Richtmyer–Meshkov instability when a shock is reflected. *Phys. Rev. E* **63**, 56303.
- WOUCHUK, J. G. 2001*b* Growth rate of the Richtmyer–Meshkov instability when a rarefaction is reflected. *Phys. Plasmas* **8**, 2890–2907.
- YOUNGS, D. L. 1994 Numerical simulation of mixing by Rayleigh–Taylor and Richtmyer–Meshkov instabilities. *Laser Part. Beams* **12**, 725–750.
- ZABUSKY, N. J., KOTELNIKOV, A. D., GULAK, Y. & PENG, G. 2003 Amplitude growth rate of a Richtmyer–Meshkov unstable two-dimensional interface to intermediate times. *J. Fluid Mech.* **475**, 147–162.
- ZHANG, Q. & SOHN, S.-I. 1997 Nonlinear theory of unstable fluid mixing driven by shock waves. *Phys. Fluids* **9**, 1106–1124.